JMEPEG
https://doi.org/10.1007/s11665-024-09787-8

1059-9495/$19.00

ORIGINAL RESEARCH ARTICLE

Effect of Isothermal Ageing on Microstructure and Corrosion Behavior of Nickel and Molybdenum-Free High Nitrogen Austenitic Stainless Steel

Surjan Sheik and Raffi Mohammed

Submitted: 25 September 2023 / Revised: 4 May 2024 / Accepted: 17 May 2024

This study investigates the influence of isothermal ageing (550–850 °C) and time (30, 60, 180, 360, 720, and 1440 minutes) on microstructure and corrosion behavior of nickel and molybdenum-free high nitrogen austenitic stainless-steel (HNASS). In solution-annealed conditions, the HNASS has a single-phase austenite structure with annealed twins at the grain boundaries. HNASS treated to the aging range at lower temperatures and shorter duration resulted in various fine, discrete, and globular chromium-nitride (Cr_2N) precipitation at grain boundaries. Whereas increased aging temperature and prolonged exposure duration led to the lamellar Cr2N pearlite-like microstructure formed within the austenite grain when treated at 650 °C, 750 °C, and 850 °C after 360 min, 180 min, and 60 min, respectively. The data obtained in potentiodynamic polarization (PDP) and double loop electrochemical potentiokinetic reactivation (DL-EPR) studies show a higher susceptibility to pitting and intergranular corrosion (IGC) with increased aging temperature and exposure duration. However, resistance to IGC and pitting corrosion of HNASS is correlated with the shape and size of Cr_2N precipitation formed at the grain boundaries and extended into the matrix. The U-bend stress corrosion cracking (SCC) studies showed that the HNASS specimen aged at 750 °C for 1 hour showed no visible cracks. However, some random pit initiation and growth were observed over a period of time when exposed for 150 hours to boiling $MgCl_2$ solution.

Keywords double loop electrochemical potentiokinetic reactivation (DL-EPR), intergranular corrosion (IGC), nickel and molybdenum-free high nitrogen austenitic stainless-steel (HNASS), potentiodynamic polarization (PDP), stress corrosion cracking (SCC)

1. Introduction

Stainless steel with nitrogen (N) content of more than 0.4% (mass per cent) in an austenitic matrix is referred to as high-nitrogen austenitic stainless steel (HNASS). These categories of stainless steel are considered strategic materials for various industries, including defence, chemical, petrochemical, thermal power, nuclear, oil, and refineries, owing to their exceptional fabrication, mechanical, and corrosion characteristics in highly aggressive environments (Ref 1-4]. Nitrogen and manganese replace more expensive nickel as austenite-stabilizing alloying elements in austenitic stainless steel (ASS), significantly reducing the material cost (Ref 5-7]. HNASS is superior to most conventional ASS due to the addition of nitrogen, which enhances grain refinement, improved strength, and solid solution strengthening without compromising toughness. The tensile and yield strengths of HNASS can surpass 200-350% of conventional AISI300 and AISI200 stainless steels (Ref 8-11] and improve resistance to localized corrosion of ASS in annealed conditions (Ref 12-18].

Prolonged exposure to these steels at temperatures between 400 °C and 900 °C may induce chromium-rich carbides or nitrides ($M_{23}C_6$/M_2N) along the grain boundaries, substantially affecting strength and corrosion characteristics (Ref 19-22]. The formation of M_2N precipitate is influenced by differences in composition and temperature, resulting in various morphologies. Previous studies reported that the formation of M_2N precipitates primarily occurs along the grain boundaries, subsequently expanding into the interior of the grains. Various chemical compositions in the alloy at different temperatures and time durations exhibit the presence of granular, rod-like, cellular, and lamellar-type M_2N precipitates (Ref 23-27]. Krishna Kumar K et al. found that various types of nitride precipitates, such as discrete disk-shaped nitrides, lenticular, and distinct needle-shaped nitrides at ageing temperatures of 900, 800, and 700 °C respectively, for a duration of 14 h in Fe-22Mn-17Cr-0.56 N steel. It was also observed that higher pitting resistance at ageing temperatures of 800 and 900 °C could be owing to disc-shaped nitrides (Ref 28]. Shi et al. (Ref 29] studied the behavior of precipitation characteristics of the Fe-18Mn-18Cr-0.63N steel and found that Cr_2N was the primary precipitate. Yanxin Qiao et al. investigated that ageing leads to the Cr2N precipitation along the grain boundaries in Fe-15Mn-18Cr-0.66N stainless steel. The morphology of the nitride precipitation transformed from dispersive particles to a continuous network at an ageing temperature of 900 °C for a 60-minute duration. It was also observed that ageing treatment significantly reduced pitting potential and shrinkage in the

Surjan Sheik and **Raffi Mohammed**, Department of Metallurgical and Materials Engineering, National Institute of Technology Andhra Pradesh, Tadepalligudem, A.P. 534101, India. Contact e-mail: raffia.u@gmail.com.

Published online: 02 July 2024

passive region in a 3.5 wt.% chloride environment (Ref 30]. Li et al. (Ref 31] found cellular Cr_2N precipitates in the Fe-16Mn-18Cr-2Mo-1.1N steel when isothermal ageing at 850 °C for 30 sec, and the fraction of these precipitates increased gradually with ageing duration. Hu et al. (Ref 32] discovered that the morphology, distribution, content, and size of Cr_2N precipitates closely correlated with the percentage of N in the HNASS. Li et al. (Ref 33] investigated the intergranular corrosion (IGC) behavior of high nitrogen austenitic stainless steel Fe-20Cr-19Mn-2Mo-0.8N (HNSS) under different sensitizing temperatures 650-950 °C for 2 h. At higher sensitizing temperatures (900 and 950 °C), the precipitation of Cr_2N along grain boundaries gradually decreases. At these higher temperatures, a reduction in the extent of intergranular Cr_2N precipitation is observed compared to lower temperatures. Lee (Ref 34] studied the morphological changes of the Fe-21Ni-22Cr-6Mo-(N) steel when isothermally aged at 900 °C and discovered that the secondary precipitates were $M_{23}C_6$ / M_6C carbide-type precipitates, whereas a low fraction of Cr_2N precipitates were found in the Fe-21Ni-22Cr-6Mo-0.3N steel after 24 hours of ageing. In contrast, Cr_2N phases typically precipitated in austenitic Fe-Cr-Mn-N stainless steel during ageing from 700 to 1000 °C (Ref 35]. These stainless steels have been shown to provide good stress corrosion cracking (SCC) resistance in various aggressive environments compared to conventional austenitic stainless steel (Ref 36, 37]. Raffi Mohammed et al. (Ref 38] studied the SCC behavior of gas tungsten arc (GTA) welded HNASS with different filler materials and found that welded with PH 13-8 Mo filler resulted in a better combination of mechanical properties and corrosion resistance when compared to GTA welds made with 11-10 PH and MDN 250 fillers. Yoon et al. (Ref 39] investigated the effect of N and C on the SCC susceptibility of Fe-18Cr-10Mn alloy and observed that the resistance to pitting corrosion initiation and the passivation kinetics due to the beneficial alloying elements of N and C.

The literature shows that several alloy compositions were developed as 'high nitrogen steels', and similar studies have been reported. However, the majority of them are Mo-bearing HNASS (Ref 40-42], but the research literature on Ni and Mo-free HNASS is very scarce (Ref 29, 30]. Since these alloys are an important class of materials for structural applications at higher temperatures, it is essential to understand the influence of the elevated temperatures for more prolonged exposure on the microstructure and corrosion behavior. Hence, an attempt is made to study the effect of isothermal ageing at the sensitization range (550-850 °C) for an exposure duration of (30-1440 min) of Fe−18Cr-20Mn-0.5N austenitic stainless steel.

2. Materials and Methods

The high nitrogen austenitic stainless steel (HNASS) of 5 mm thickness was used in the present study, and the elemental composition of HNASS is given in Table 1. Initially, the HNASS in as-received condition was solutionized at 1100 °C for 2 hours, followed by a water quench. The solutionized specimens were subjected to isothermal ageing in the sensitization temperature range i.e., 550 °C, 650 °C, 750 °C, and 850 °C for 30 min, 60 min, 180 min, 360 min, 720 min, and 1440 min. The above ageing treatments were done to study and determine the effect of isothermal aging on microstructural morphology, pitting corrosion, and intergranular and stress corrosion cracking resistance. A wire-electrical discharge machine (W-EDM) is used to cut the specimens of the required dimensions, i.e., 10x10x5 mm^3. The sectioned specimens were polished using a series of emery papers and

Table 1 Elemental composition of nickel and molybdenum-free high nitrogen austenitic stainless-steel (HNASS)

	Element wt%										
Material	**Cr**	**Mn**	**C**	**N**	**P**	**S**	**Mo**	**Ni**	**Si**	**Fe(balance)**	**Cr^{eff}**
HNASS	17.96	19.78	0.076	0.543	0.051	0.007	-	-	0.34	61.243	17.8522

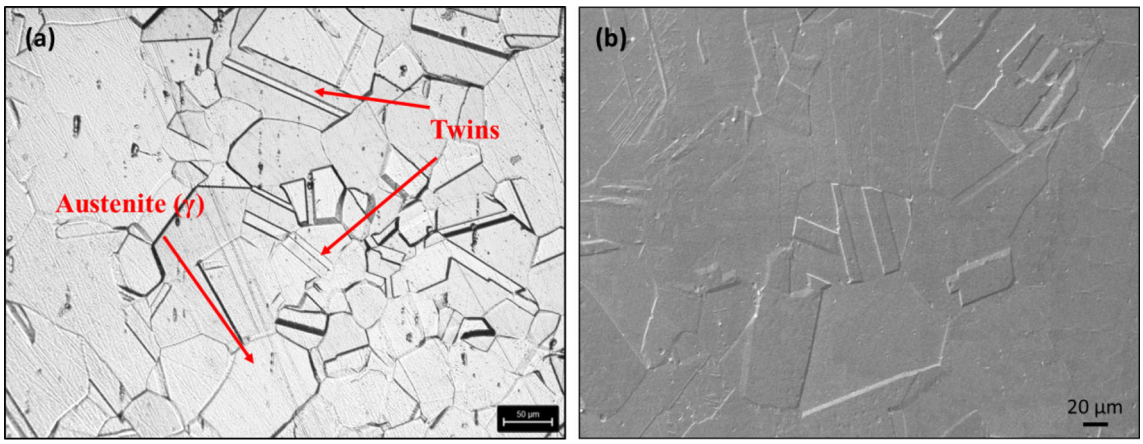

Fig. 1 Solutionized microstructure of HNASS at 1100 °C for 2 hours (a) optical micrograph (b) SEM micrograph

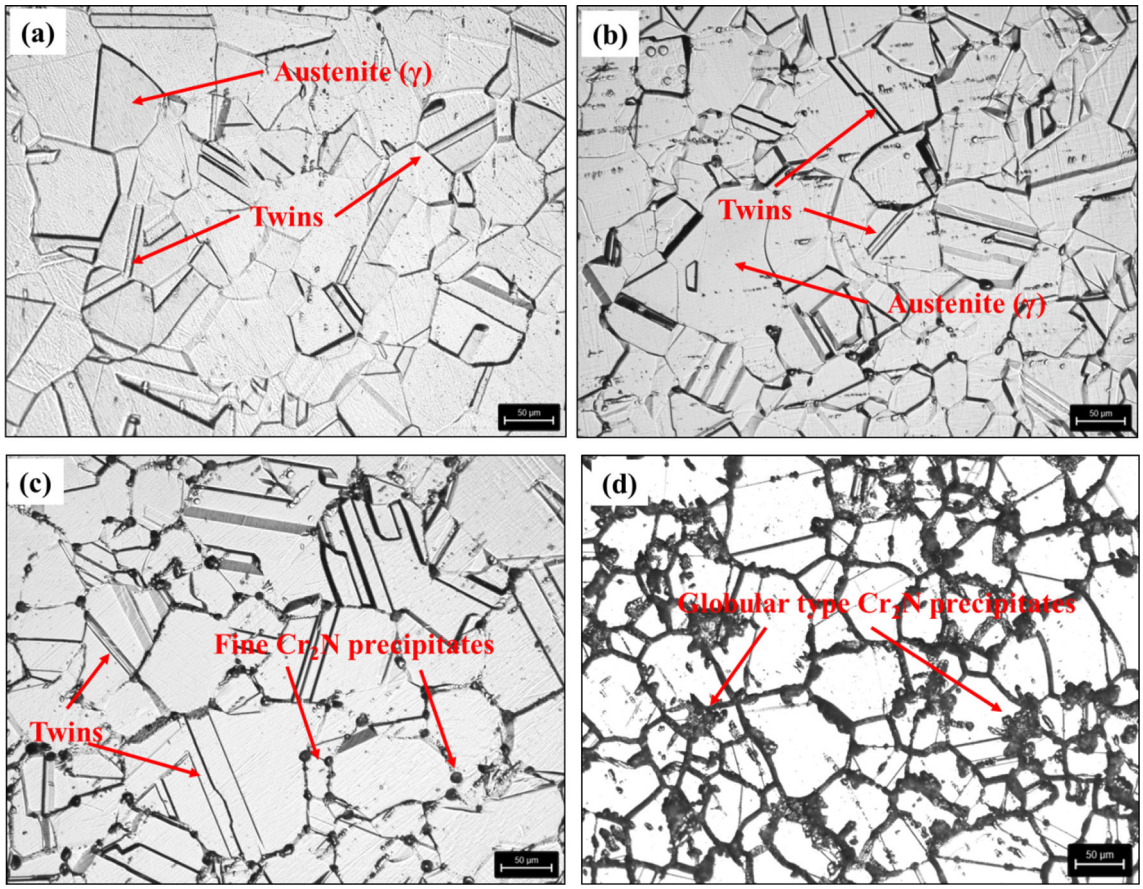

Fig. 2 Optical microstructures (200x magnification) of HNASS specimens aged for 30 minutes at different temperatures (a) 550 °C (b) 650 °C (c) 750 °C and (d) 850 °C

disc polish using 0.75μ alumina powder for morphological and electrochemical studies. The qualitative analysis of the solutionized and aged HNASS specimens was evaluated following the ASTM A262 standard Practice A. Using an electrolytic cell, all the specimens are electrochemically etched for 90 seconds in a solution of 10% oxalic acid with a 1 A/cm^2 current density. The microstructural examinations of the specimens were recorded using a LEICA high-resolution optical microscope with image analysis software. Energy dispersive spectroscopy, coupled with the Scanning Electron Microscope (ZEISS EVO Series Model EVO 18) and Oxford- Energy Dispersive X-ray system (INCA 250 EDS with X-MAX 20 mm Detector), was used to scan the elemental composition of the precipitates across the grain boundaries. The phases of HNASS are identified using the X-ray diffractometer (Ultima IV, Rigaku, Japan) with a Cu Kα X-ray source (k = 1.5405 Å), operating at 40 kV and 30 mA.

For corrosion studies, a basic 3-electrode electrochemical system (GillAC serial No-1937 sequencer) was used with the working electrode as the treated specimen, the reference electrode as the saturated calomel electrode, and the auxiliary electrode as the platinum. The specimen (working electrode) was kept in the same solution for 30 min till the rest potential was attained. Then, it was anodically polarized in forward and reverse scan with a scan rate of 100 mV/min from rest potential to 300 mV (vs. Ref) and vice versa. Double loop electrochemical potentiokinetic reactivation (DL-EPR) tests are conducted in an electrolytic solution containing 0.5 M sulphuric acid (H_2SO_4) + 0.01 M potassium thiocyanate (KSCN) as per ASTM G 108 standard (Ref 43]. The degree of sensitization (%DOS) is calculated by the ratio of reactivation current density (I_r) to the activation current density (I_a) (Ref 44]. Potentiodynamic polarization (PDP) tests are performed in an aerated 3.5% NaCl solution to understand the pitting corrosion properties of HNASS at various conditions. The stress corrosion cracking (SCC) test was carried out in a boiling 45% magnesium chloride ($MgCl_2$) solution boiling at 155 °C as per ASTM G36 (Ref 45] on the U-bend specimen prepared according to ASTM G 30-94 and treated at 750 °C for 1 hour (Ref 46].

3. Results and Discussion

3.1 Microstructural Observation

Figure 1 depicts the optical and scanning electron micrographs of high nitrogen austenitic stainless-steel (HNASS) solutionized at 1100 °C for 2 hours after etching as per the ASTM A262 Practice A standard. It was found that HNASS has a fully austenitic (γ) phase with annealed twins near the grain boundaries (Ref 47], and no traces of carbides or nitrides are found along the grain boundaries. As depicted in Fig. 12, the X-ray diffraction pattern of the HNASS also found that it has only a single austenitic phase in solutionized condition.

3.2 Effect of Isothermal Aging on Cr_2N Precipitation

3.2.1 Oxalic Acid Etch Test Results. The sensitization tendencies of austenitic stainless steels are mainly influenced by the alloy composition. Chromium and carbon are the primary alloying elements that impact carbide precipitation at the grain boundaries. The alloy's effective chromium concentration (Creff) was computed using an equation suggested by parvathavarthini (Ref 48], which influences the sensitization behavior during isothermal ageing.

$$\begin{aligned} Cr^{eff} = & Cr - 100C + 1.45Mo + 0.13Mn + 9.2N \\ & - 0.19Ni - 0.22Si - 020Co - 0.51Al \\ & + 0.01Cu + 0.34V + 0.61Ti - 0.22W \end{aligned}$$

To analyse qualitatively, ASTM A262 Practice A standard was used to understand the sensitization behavior of HNASS during isothermal ageing. The microstructural morphology of aged HNASS was categorized as follows after conducting an etch test as per standard:

1) The step structure only includes steps among the grains, with no ditches present at the grain boundaries.

2) Dual structure, with some ditches and steps present at the grain's boundaries, but no grain is enclosed by ditches in any direction.

3) The ditch structure consists of at least one grain surrounded by ditches.

Figures 2, 3, 4, 5, 6, 7 illustrates the HNASS morphological changes, such as the formation of Cr_2N precipitation and its growth during isothermal aging at 550 °C to 850 °C for 30, 60, 180, 360, 720 and 1440 minutes exposure durations. The austenitic (γ) phase was the prevailing phase observed in the HNASS at solutionized conditions, along with the presence of

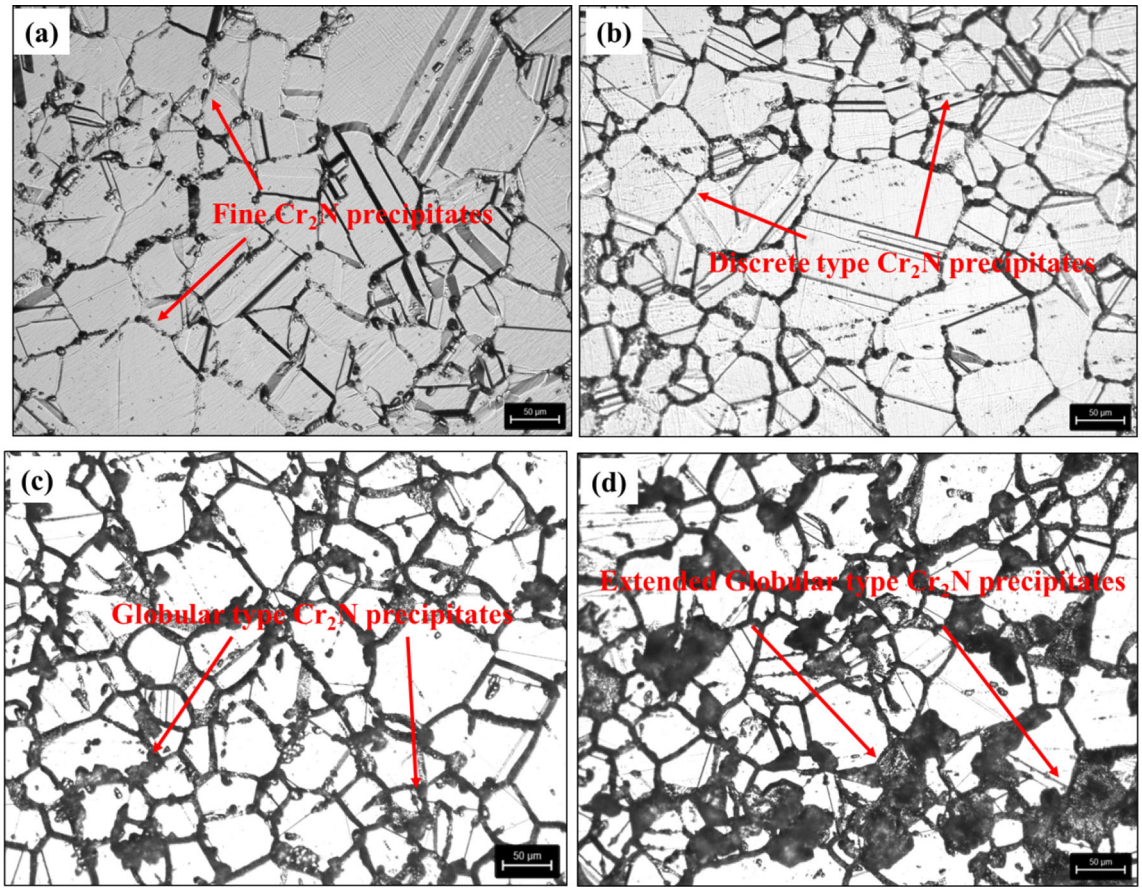

Fig. 3 Optical microstructures (200x magnification) of HNASS specimens aged for 60 minutes at different temperatures (a) 550 °C (b) 650 °C (c) 750 °C and (d) 850 °C

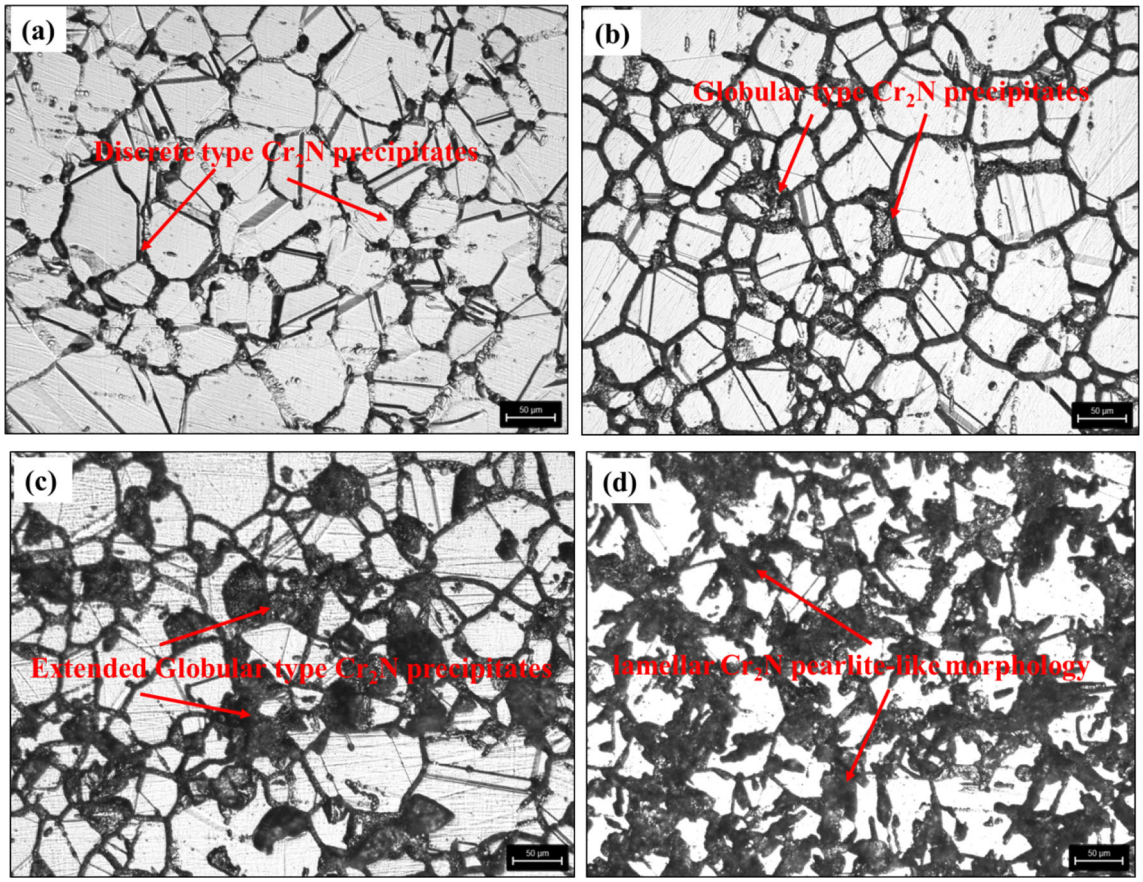

Fig. 4 Optical microstructures (200x magnification) of HNASS specimens aged for 180 minutes at different temperatures (a) 550 °C (b) 650 °C (c) 750 °C and (d) 850 °C

annealing twins within the γ grains. The microstructure varies as the solutionized specimen is treated to isothermal aging conditions. The secondary phase volume spreads from grain boundaries into grain interiors, forming a lamellar pearlite nature of precipitation as the exposure duration increases. The step-like structure was observed at lower sensitization ranges, i.e., 550 °C and 650 °C, as shown in Figs. 2a, b, 3a and 4a, which shows the initiation of nitrides precipitation at the grain boundaries and leads to step structure. It is observed that HNASS during the exposure duration of 30 min, 60 min, and 180 min at 550 °C and 30 min at 650 °C have resulted in the initial stage of precipitation and random distribution of Cr_2N precipitation at grain boundaries. Where the "dual- structure" was observed for 60 min at 650 °C and 30 min at 750 °C and 850 °C, precipitation of nitrides was initiated at the grain boundaries and as shown in Figs. 2c, d, 3b and 5a. As exposure duration at higher sensitization temperatures increases, more severe nitride precipitation and thickening of grain boundaries are observed. The shorter exposure at a lower sensitization range, i.e., 60 minutes at 550 °C and 650 °C, is inadequate for HNASS to have susceptibility to intergranular corrosion. However, precipitation is more aggressive at shorter exposure at higher sensitization range, i.e., 60 min at 750 °C and 850 °C, unlike their lower sensitization range. This could be attributed to the increased driving force for higher nucleation rates, which leads to higher precipitation tendencies during the initial exposure durations at higher temperatures. Whereas shown in Figs. 4d, 5c, d, 6b,c,d and 7b, c, d that the chromium nitrides are precipitated near all the grain boundaries and lead to a "ditch" structure.

The mechanism of precipitate transformation during isothermal ageing is relatively complex. The precipitation occurs not only at the grain boundary but also at the interior of the grains. At isothermal range temperatures for lower exposure duration has led to the development of fine, discrete, and globular Cr_2N precipitation at grain boundaries, as shown in Figures 2, 3, 4, 5, 6, 7. Further rise in ageing temperature and exposure duration (i.e., 360 min at 650 °C, 180 min at 750 °C and 60 min at 850 °C) leads to the increase in the fraction of extended globular precipitates and initiates the lamellar Cr_2N pearlite-

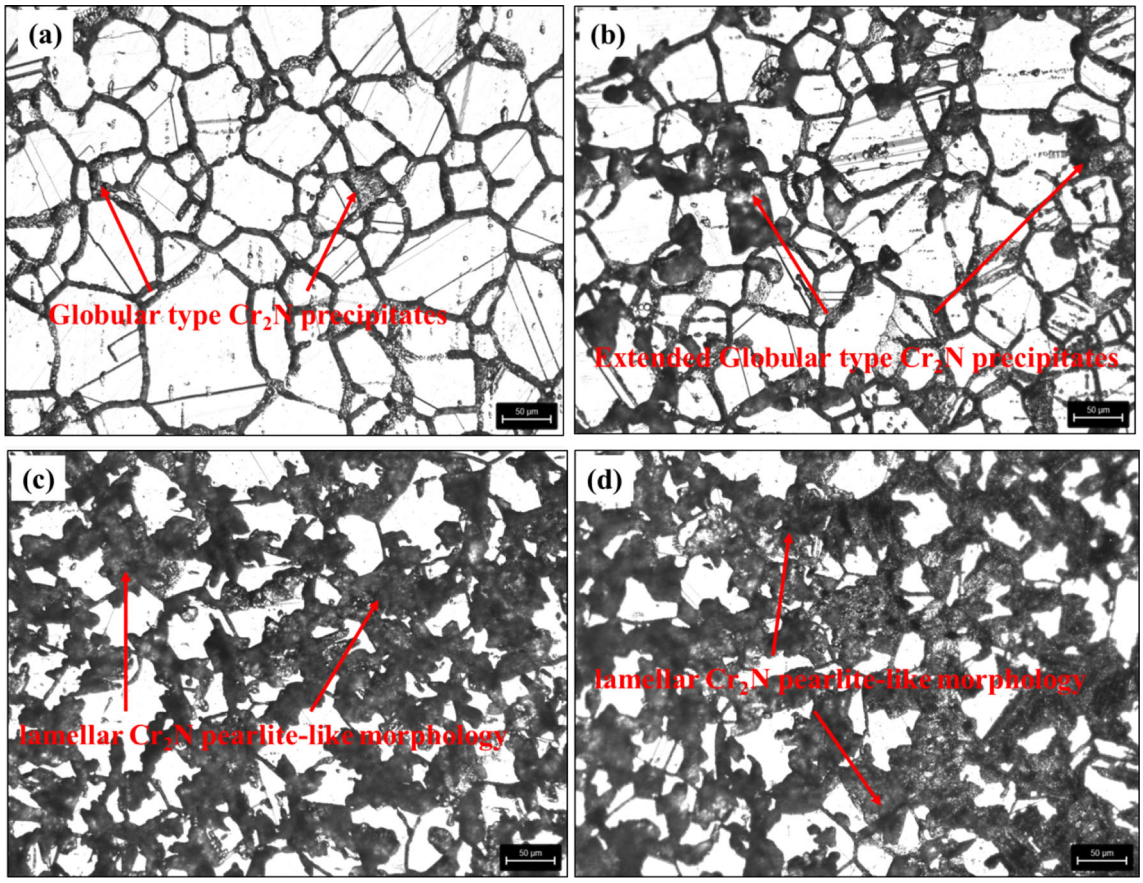

Fig. 5 Optical microstructures (200x magnification) of HNASS specimens aged for 360 minutes at different temperatures (a) 550 °C (b) 650 °C (c) 750 °C and (d) 850 °C

like morphology in the austenite crystal. As shown in Figs. 3d, 4c and 5b at 850 °C after 60 min, at 750 °C after 180 min, and at 650 °C after 360 min of ageing, the dispersed particles observed in the microstructure of the cellular precipitate transform to lamellae Cr_2N pearlite-like microstructure.

Figure 8 depicts the experimentally obtained temperature-time-sensitization curve, which summarizes the effect of the isothermal ageing temperature range on the microstructural features of HNASS. The microstructural features during various ageing treatments are separated into three groups illustrated by the scanning electron microscopy (SEM) in Fig. 8. The black coloured curve divides the sensitization-free area from the temperature-time region containing visible precipitates of Cr-rich nitrides within the micrographs. The initial precipitates were identified at the grain boundaries at various aging temperatures and durations, such as at 550 °C after 180 min, 650 °C after 60 min, and 750 °C and 850 °C after 30 min. These precipitates in the austenite solid solution originated from the supersaturation of carbon (0.07 wt %) and nitrogen (0.54 %). However, Cr-rich nitrides of the M_2N type were the dominating secondary phase in the microstructure at aging temperatures.

The specimens subjected to ageing at temperatures of 550 °C, 650 °C, 750 °C and 850 °C for a different time duration dominantly detected secondary phase in the microstructure was Cr-rich nitrides of the M_2N type at the grain boundaries. At elevated ageing temperatures, many nitrides occupy the grain boundaries. Further, starting from 650 °C for 720 min, Cr_2N precipitation occurs in the interior of the grain. At 750 °C, this takes place after 180 min, but at 850 °C, it starts after 60 min. Figure 9 shows the SEM micrograph of the HNASS aged at 850 °C for 1440 min of duration. As the exposure duration increases, the precipitates form in cellular morphology, preliminary from the grain boundaries into the interior of the austenite grain, which can be seen in the SEM micrograph. Some researchers observed distinct disk-shaped nitrides, lenticular, and needle-shaped nitrides at ageing temperatures of 900, 800, and 700 °C for 14 hours at the grain boundaries (Ref 28]. Fine, globular, and plate-like precipitates were found for a longer ageing duration of 200 h at a temperature of 850 °C (Ref 24]. The addition of molybdenum into HNASS also influences the formation of different intermetallics such as grain boundary Cr_2N, cellular Cr_2N, σ -phase, and chi (χ) + M_7C_3 carbide precipitates were observed at different temperatures and longer aging durations (Ref 29, 41]. The effect of this cellular morphology of Cr-nitride precipitation on the localized corrosion characteristics of the HNASS has been studied at higher temperatures and time durations.

3.2.2 Scanning Electron Microscopy (SEM) and Energy Dispersive Spectroscopy (EDS) Observations. Figures 10 and 11a, b represent the SEM images with line-scan graphs of the HNASS specimens aged at 550 °C for 60 min and 850 °C

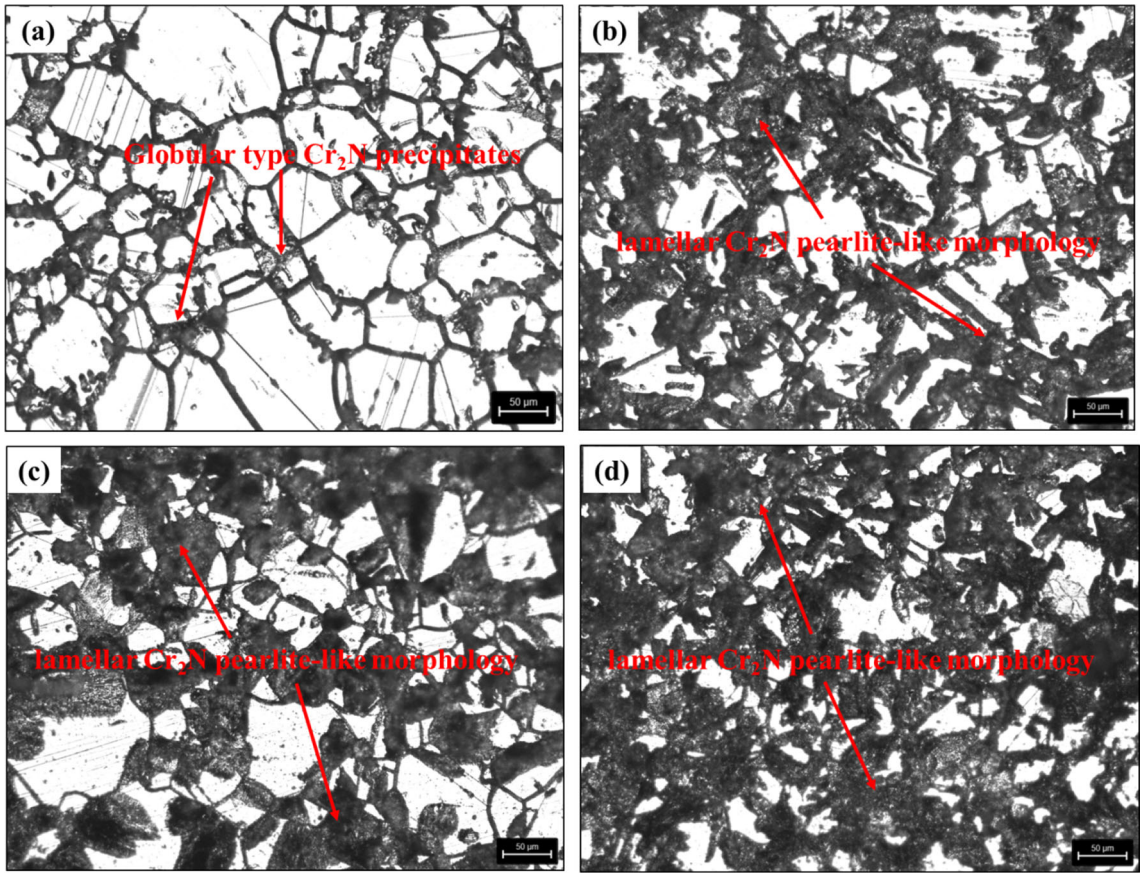

Fig. 6 Optical microstructures (200x magnification) of HNASS specimens aged for 720 minutes at different temperatures (a) 550 °C (b) 650 °C (c) 750 °C and (d) 850 °C

for 1440 min. The line scan across the grain boundary revealed the existence of Cr-rich nitrides near the grain boundary. To further examine the elemental composition of the precipitates across the grain boundary, EDS investigated the precipitates, and the findings are shown in Figs. 10c and 11c. EDS results showed that the precipitates have more Fe, Mn, and Cr, showing that the precipitates in the ageing treatment of HNASS are M_2N and $M_{23}C_6$ type precipitates at the grain boundaries. The EDS examination of the grain boundary precipitates (Fig. 10) reveals that they are rich in N and Cr, whereas the EDS examination of lamellar Cr_2N pearlite-like precipitates (Fig. 11) are rich in Fe, Cr, and Mn.

Initial observations indicate that Cr_2N precipitation initiates at grain boundaries. As the exposure time increases, the quantity of Cr_2N precipitation increases to the point where the grain boundaries are nearly covered, as depicted in Figures 3, 4, 5, 6, 7. At 850 °C for lower ageing durations, the intergranular precipitation continues to coarsen, and cellular Cr_2N lamellae precipitate initially along the grain boundaries with a tiny cellular region, as seen in Figs. 2d and 3d. As illustrated in Fig. 11a & b, the cellular zone widens when the ageing temperature increases to 850 °C for 1440 minutes duration, resulting in multiple locations within grains covered with cellular Cr_2N precipitation. Zou Zhangxiong et al. (Ref 49] discovered that in specimens aged above 800 °C, the structure of Cr_2N precipitates formed in 0.7N38K ASS represents a pearlite-like microstructure. It is simple for nitrogen to agglomerate closer to the grain boundary due to its highly active nature at the boundary. At the appropriate temperature for ageing, the nitrogen can readily combine with the chromium to form Cr_2N, which can then precipitate on the grain boundary. This trend is more significant when the nitrogen level is higher, and it is much simpler to precipitate nitride in these conditions.

Figure 12 depicts the XRD results of the HNASS in solutionized condition, isothermally aged at 550 °C for 60 min and 850 °C for 1440 min. From the results, it is observed that the HNASS has a single austenitic phase in solutionized condition. In aged conditions at 550 °C for 60 min and 850 °C for 1440 min, the precipitates in HNASS steel are the Cr_2N phase. The XRD results are coincident with the SEM and EDS observations. Similar results are broadly consistent with the previous reports on alloys with comparable properties (Ref 29, 50].

3.3 Effect of Isothermal Ageing on Degree of Sensitization

The DL-EPR curves of HNASS aged at 550 °C to 850 °C for various exposure durations are depicted in Fig. 13. The current densities of the activation peak (I_a), reactivation peak

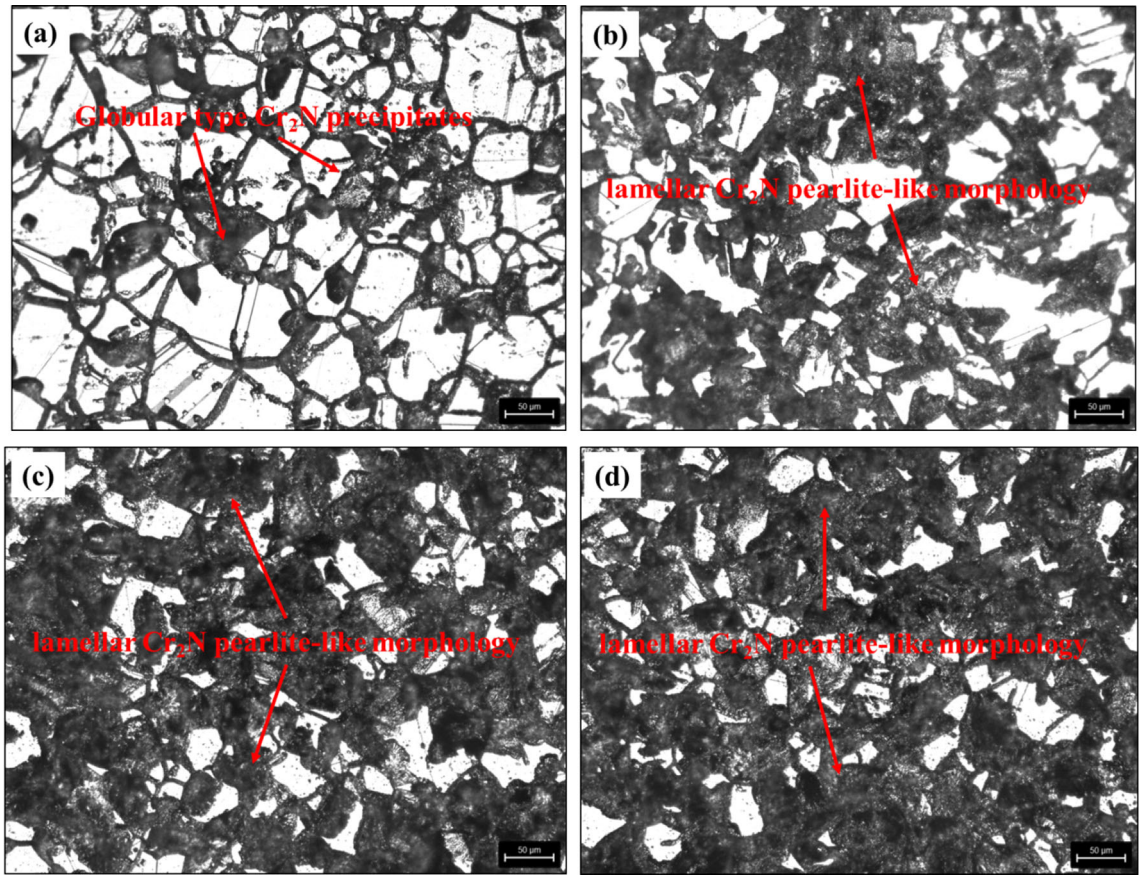

Fig. 7 Optical microstructures (200x magnification) of HNASS specimens aged for 1440 minutes at different temperatures (a) 550 °C (b) 650 °C (c) 750 °C and (d) 850 °C

Table 2 Results obtained in ASTM A262 Practice A test and DL-EPR data of HNASS

Isothermal aging condition	Obtained results as per ASTM A262 practice A	I_r, mA/cm^2	I_a, mA/cm^2	% Degree of sensitization (DOS)
Solutionized at 1100 °C for 2hrs.	Step	0.05	5.39	0.93
Aging at 550 °C-30 min	Step	0.29	5.32	5.45
Aging at 550 °C-60 min	Step	0.54	4.28	12.62
Aging at 550 °C-180 min	Step	0.94	5.22	18.01
Aging at 550 °C- 360 min	Dual	1.15	3.90	29.49
Aging at 550 °C-720 min	Dual	1.73	5.13	33.72
Aging at 550 °C-1440 min	Dual	1.80	4.27	42.15
Aging at 650 °C-30 min	Step	0.54	5.89	9.17
Aging at 650 °C- 60 min	Step	0.81	4.03	20.10
Aging at 650 °C-180 min	Dual	1.46	5.60	26.07
Aging at 650 °C-360 min	Dual	1.80	4.98	36.14
Aging at 650 °C-720 min	Ditch	2.09	5.01	41.72
Aging at 650 °C- 1440 min	Ditch	2.44	5.05	48.32
Aging at 750 °C- 30 min	Step	0.64	5.37	11.92
Aging at 750 °C-60 min	Dual	0.88	5.20	16.92
Aging at 750 °C-180 min	Dual	1.86	6.37	29.20
Aging at 750 °C- 360 min	Ditch	1.44	4.08	35.29
Aging at 750 °C-720 min	Ditch	2.07	4.17	49.64
Aging at 750 °C-1440 min	Ditch	2.01	4.27	47.07
Aging at 850 °C-30 min	Step	0.90	5.54	16.25
Aging at 850 °C-60 min	Dual	1.20	5.45	22.02
Aging at 850 °C-180 min	Ditch	1.74	4.92	35.37
Aging at 850 °C-360 min	Ditch	2.08	5.09	40.86
Aging at 850 °C-720 min	Ditch	2.58	4.91	52.55
Aging at 850 °C-1440 min	Ditch	1.97	4.51	43.68

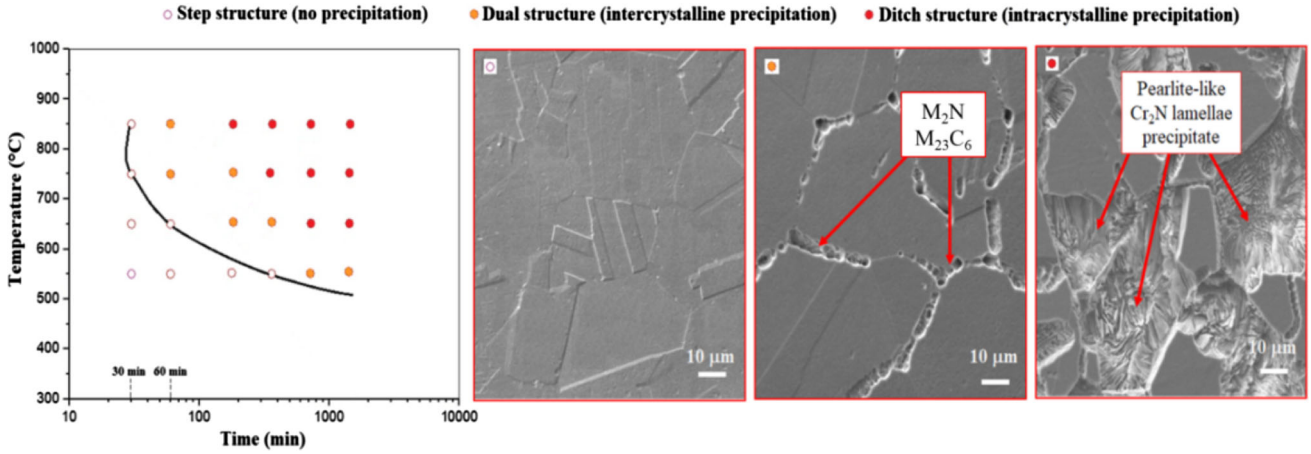

Fig. 8 Temperature-time-sensitization diagram following ASTM A262 practice A and SEM microstructures showing the formation of M_2N/$M_{23}C_6$, and pearlite-like Cr2N lamellae precipitate during the aging of HNASS

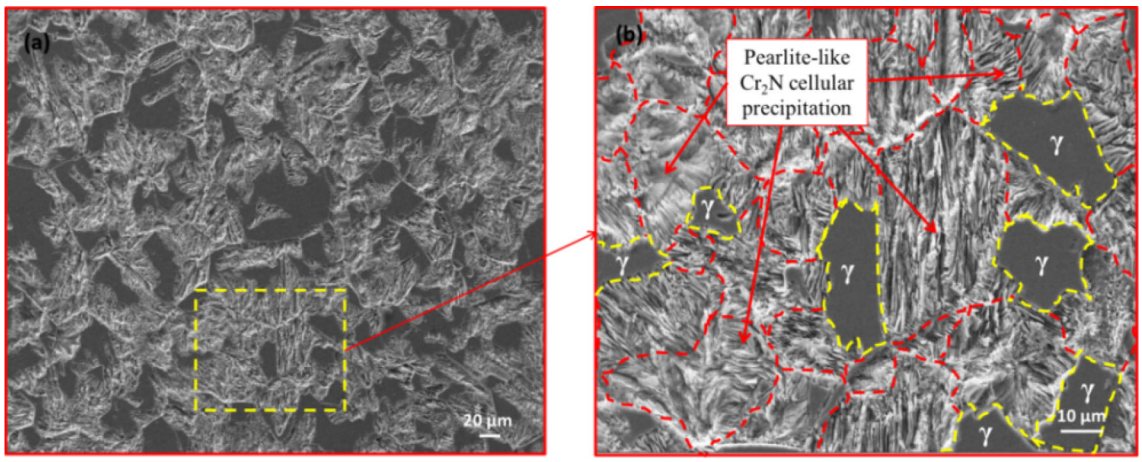

Fig. 9 SEM micrograph of the intragranular growth of cellular Cr_2N pearlite-like precipitates after being aged HNASS at 850 °C for 1440 min

(I_r), and the percentage of the degree of sensitization (% DOS) are tabulated in Table 2. The DL-EPR test found that the I_r was minimal in solutionized condition, indicating that the degree of sensitization is extremely low. This result from microstructural morphology observed in solutionized condition where HNASS has a fully austenitic phase, and no traces of nitrides or carbides are found along the grain boundaries (Fig. 1). The lack of a peak reactivation current density (I_r) at lower durations (30 min) of all temperatures suggests that the aged specimens are immune to intergranular corrosion (IGC). From the DL-EPR curves and data, it is observed that the activation current density (I_a) remained relatively constant across all time intervals at all temperatures. However, at 550 and 650 °C for longer ageing durations, an increase in ageing temperature resulted in a corresponding rise in reactivation current density. The I_r in the reverse scan could be related to the dissolution of vulnerable regions in the aged specimen, such as the Cr-depleted regions at the grain boundaries (Ref 51, 52]. This could be due to the chromium-rich nitride precipitation at the grain boundaries and further growing into the grain with extended durations at ageing temperatures, which could be observed in the optical and SEM micrographs.

Figure 15(b) shows the effect of ageing time at different temperatures on %DOS. At higher temperatures, 750 °C and 850 °C for a smaller ageing duration (30 min) were observed to have higher % DOS, whereas the same % DOS is experienced by lower aging temperature at 550 °C for 180 min. However, the significant grain boundary and cellular precipitation that occurred at 750 °C and 850 °C after 720 min of ageing duration had no impact on material ageing due to the chromium homogenization at the grain boundaries (desensitization). Due to the insufficient depletion of chromium (Cr) content caused by nitride precipitation at the abovementioned temperatures. Consequently, no attack was observed during the testing

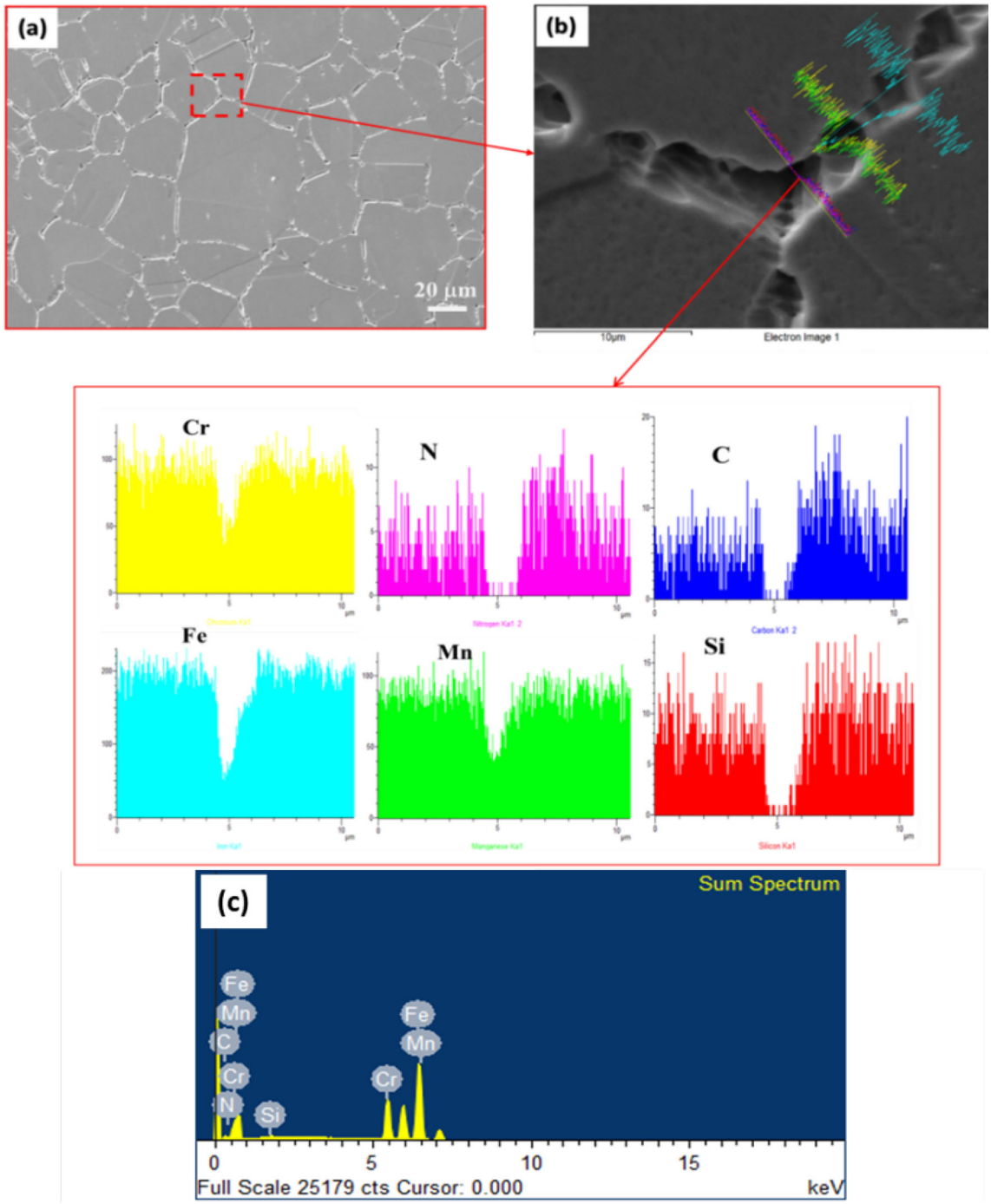

Fig. 10 (a) Scanning electron image, (b) line scan mapping analysis, and (c) EDS results of HNASS aged at 550 °C for 60 min

conducted using DL-EPR. Due to this, the Cr-depletion caused by nitride precipitation at 750 °C and 850 °C was insufficient to induce an attack. These desensitization effects at higher isothermal ageing temperatures for longer exposure durations are consistent with the previous reports (Ref 53-56].

3.4 Effect of Isothermal Ageing on Pitting Corrosion Behavior

Figure 14 depicts the potentiodynamic polarization (PDP) curves of the HNASS aged at 550 °C to 850 °C for different exposure durations. The corrosion potential (Ecorr), passive current density (Ipass), and pitting potentials (Epit) obtained

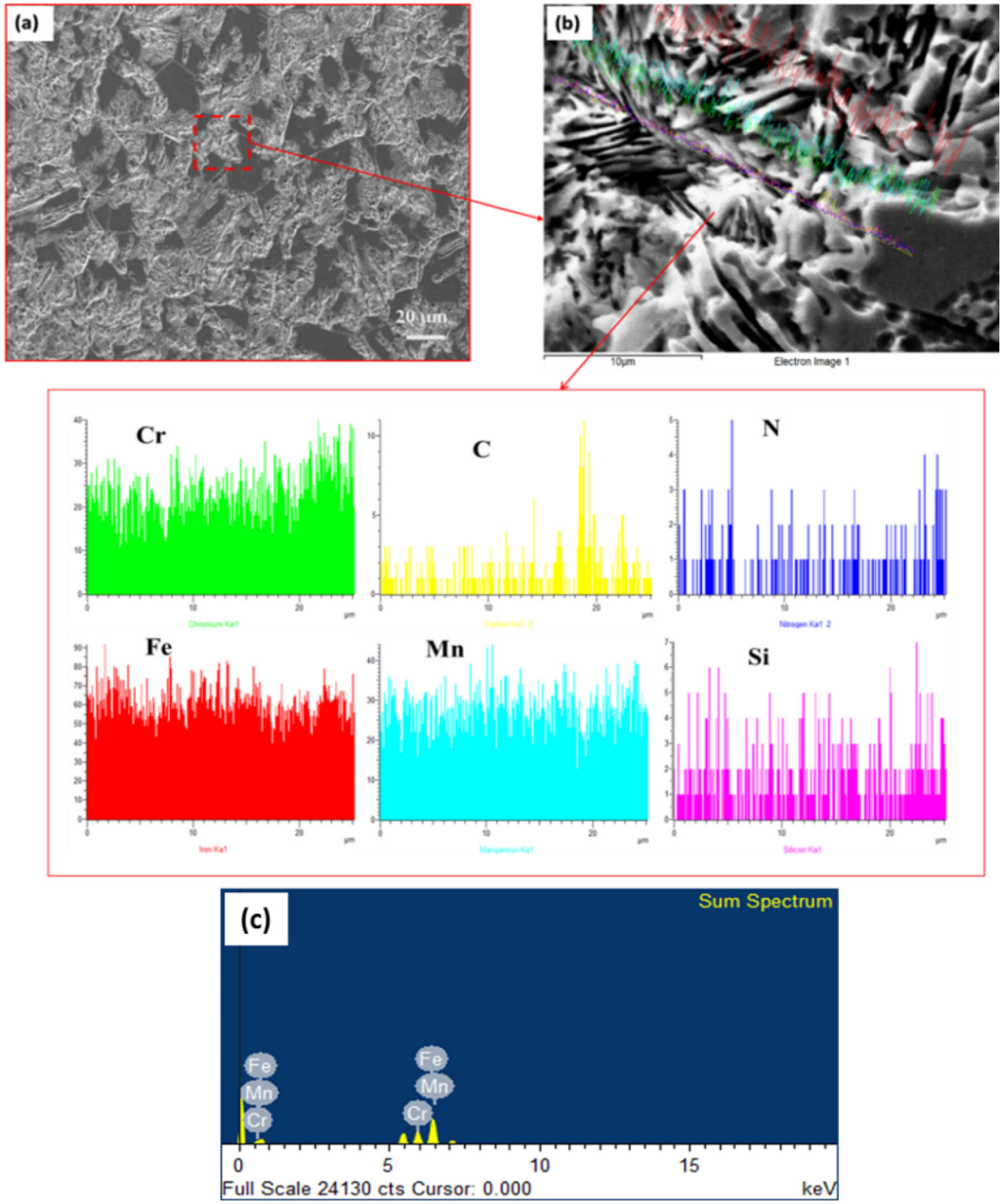

Fig. 11 (a) Scanning electron image, (b) line scan mapping analysis, and (c) EDS results of HNASS aged at 850 °C for 1440 min

from PDP curves are listed in Table 3. As shown in Fig. 14 it was observed from PDP plots that various temperatures and exposure time duration directly impact the corrosion parameters. Fig. 15(a&c) shows the effect of ageing time at different isothermal ageing temperatures on pitting potentials and passive current density. At 550 °C, as shown in Fig. 14a, that the variations in Ecorr (corrosion potential) and Ipass (passive current density) showed minimal changes across various ageing durations compared to higher ageing temperatures and durations. In contrast, the passive potential regions narrowed, and pit potentials diminished with increased ageing time as depicted in Figs. 14 and 15a, c. At this 550 °C temperature, the steel seemed less prone to sensitization effect, which typically affects the corrosion resistance of the alloy compared with the higher ageing temperatures and exposure durations. However, as the specimen is exposed to higher ageing temperatures, as illustrated in Fig. 14b, c, d, the PDP plot shifts downward and to the right, indicating that the specimens exposed to higher temper-

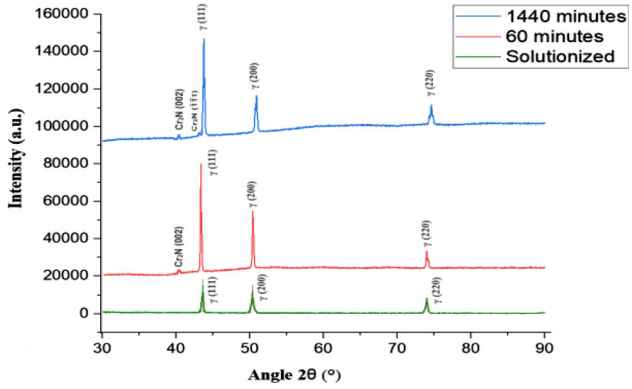

Fig. 12 XRD identification of HNASS in solutionized, aged at 550 °C for 60 min and 850 °C for 1440 min

atures have a higher corrosion rate. A sharp increase in Ipass can be noticed at higher aged temperatures due to the presence of a high fraction of Cr_2N precipitates near the grain boundary. As exposure time increased at 650 °C, the Epit shifted to more negative potentials, indicating that exposure duration influenced the pitting corrosion of HNASS. Yanxin Qiao et al. (Ref 30] found similar results for ageing-treated Mo-free high nitrogen stainless-steel in 3.5 wt% chloride solution. The fall in Epit and the reduction in the potential passive range which was attributable to a rise in the amount of precipitate inside and along the grain boundaries. However, once Cr_2N began to precipitate in the form of lamellar structure inside the crystals (aged for 720 min or longer at 650 °C), Epit changes to more negative potentials and leads to lower pitting corrosion resistance at higher ageing temperatures. The increased pitting potentials were observed at 750 and 850 °C for 1440 min

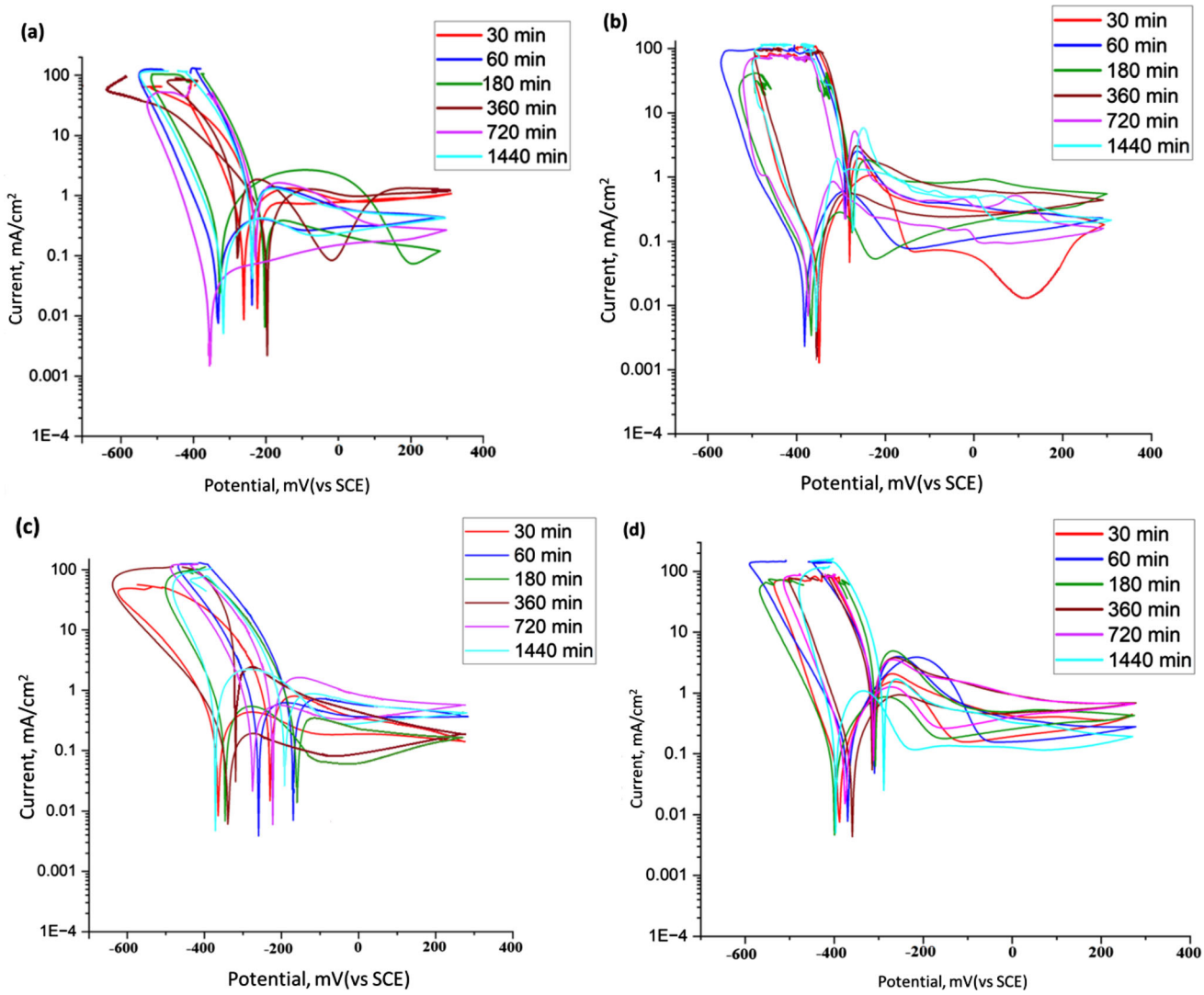

Fig. 13 DL-EPR curves of HNASS specimens aged at (a) 550 °C (b) 650 °C (c) 750 °C and (d) 850 °C for different exposure time durations

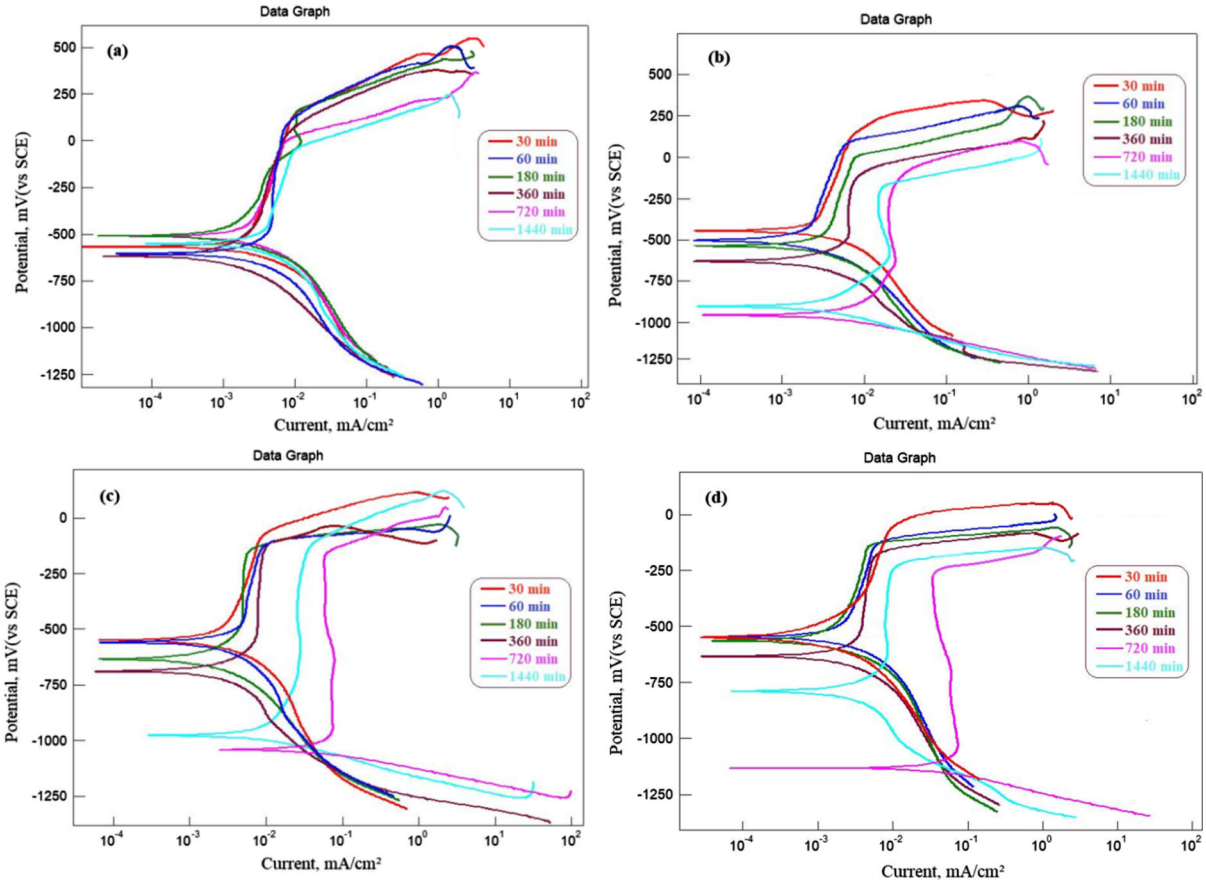

Fig. 14 PDP curves of HNASS specimens aged at (a) 550 °C (b) 650 °C (c) 750 °C and (d) 850 °C for different exposure time durations

compared to 720 min due to the chromium homogenization at the grain boundaries, which affects the corrosion behavior of the HNASS.

The alloy subjected to isothermal ageing at a temperature of 750 °C and 850 °C for a longer duration of 1440 min exhibited a significant amount of grain boundary (GB) and cellular Cr_2N precipitates compared to lower exposure durations. However, the alloy experiences a low pitting and IGC susceptibility due to insufficient chromium (Cr) content depletion caused by nitride precipitation at the abovementioned temperatures and exposure to longer durations. Hence, a significant decrease in reactivation corrosion current was observed during the DL-EPR test. According to a study by bruemmer and colleagues, the EPR test targeted chromium-depleted areas in austenitic stainless-steel with chromium concentrations ranging from approximately 12.5 wt% to 13.5 wt% (Ref 57]. Hence, the alloy exhibited lower % DOS and higher pitting potential in DL-EPR and PDP studies owing to the insufficient depletion of Cr content caused by nitride precipitation at the exposure after 720 min at 750 °C and 850 °C.

3.5 Effect of Aging Treatment at 750 °C for 1 Hour on Stress Corrosion Cracking (SCC) Behavior

The stress corrosion cracking (SCC) test was carried out on in a boiling 45% magnesium chloride ($MgCl_2$) solution boiling at 155 °C as per ASTM G36 (Ref 45]. The U-bend specimen was prepared according to ASTM G 30-94 and treated at 750 °C for 1 hour (Ref 46]. The schematic diagram and actual U bend specimen of HNASS are shown in Fig. 16.

The stress corrosion cracking (SCC) tendency of HNASS alloy was investigated in aged condition at 750 °C for 1 hour on a U bend specimen for 150 hours duration. Mn-Austenite alloy containing nitrogen around 0.5% of the initiation of precipitate formation is found above 700 °C and nearly 1 hour in duration (Ref 35]. From the microstructural observations, as shown in Figs. 3(c) & 17, it is observed that the Cr_2N precipitates began to precipitate at the grain boundaries during early stages at 750 °C for 1-hour exposure. Hence the SCC behavior of HNASS was studied at this aging temperature and exposure duration.

The surface and cross-sectional macrographs of the U bend testing specimens of HNASS aged at 750 °C for 1 hour exposed to a boiling 45% $MgCl_2$ solution for 150 hours are

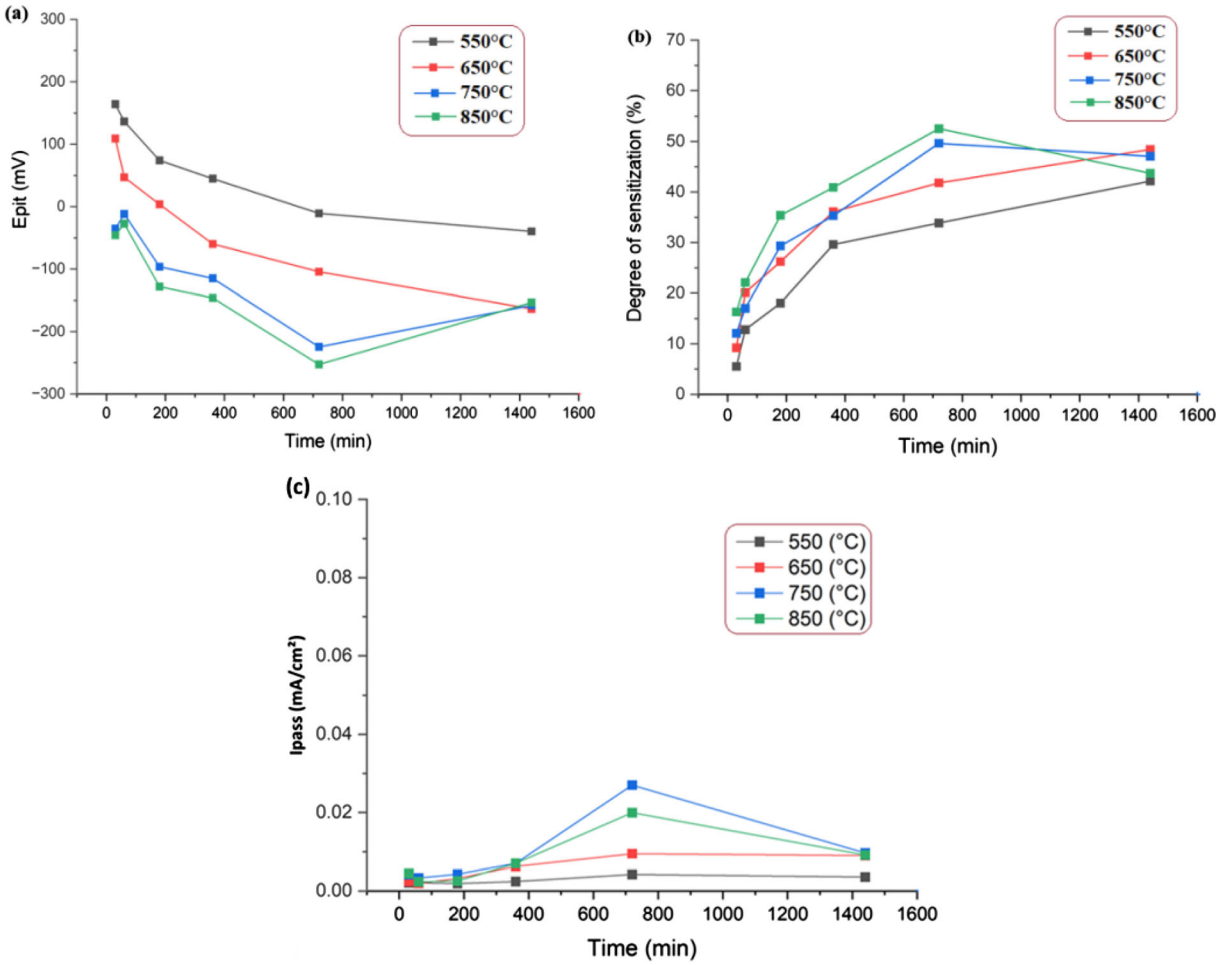

Fig. 15 Effect of exposure time at different aging temperatures on (a) pitting potentials (b) degree of sensitization (%DOS) and (c) passive current density of HNASS

Table 3 Data obtained from potentiodynamic polarization studies of HNASS

Temperature, °C	Time, min	E_{corr}, mV vs. SCE	I_{pass}, mA/cm^2	E_{pit}, mV vs. SCE
550	30	− 567	0.00203	164
	60	− 514	0.00212	136
	180	− 513	0.00189	74
	360	− 623	0.00241	45
	720	− 608	0.00418	− 10
	1440	− 549	0.00355	− 39
650	30	− 510	0.00235	109
	60	− 567	0.00197	47
	180	− 601	0.00319	4
	360	− 697	0.00625	− 59
	720	− 1023	0.00947	− 104
	1440	− 970	0.00899	− 163
750	30	− 589	0.00415	− 35
	60	− 594	0.00332	− 11
	180	− 673	0.0043	− 96
	360	− 722	0.00701	− 114
	720	− 1090	0.02702	− 224
	1440	− 1029	0.00966	− 157
850	30	− 517	0.00444	− 45
	60	− 509	0.00235	− 27
	180	− 531	0.00254	− 128
	360	− 591	0.00701	− 146
	720	− 1101	0.01994	− 252
	1440	− 742	0.00913	− 153

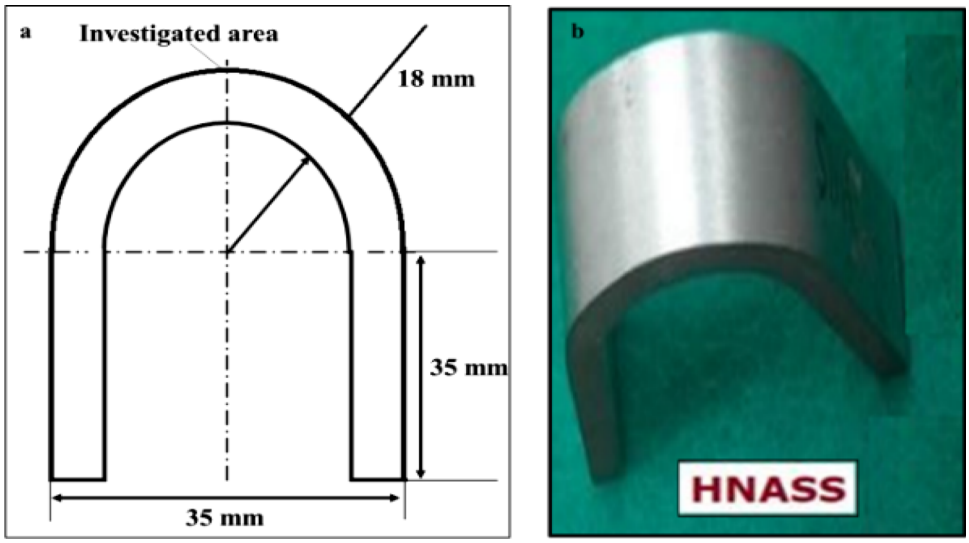

Fig. 16 (a) schematic representation of the U bend specimen and (b) actual specimen of HNASS

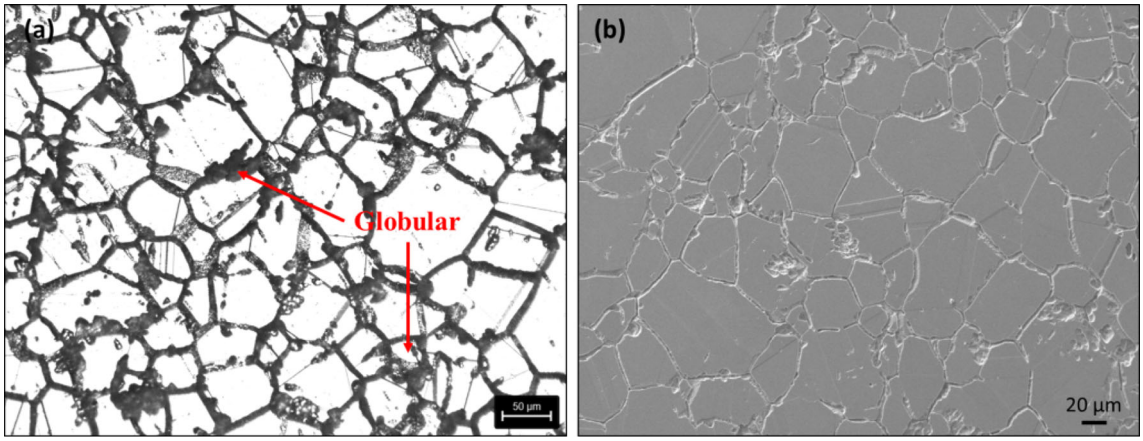

Fig.17 (a) Optical and (b) SEM micrographs of HNASS aged at 750 °C for 1 hour

shown in Fig. 18. During the entire test, no visible cracks were identified on the bent surface. The experimental results revealed that the specimen surface was not much affected after being exposed to the $MgCl_2$ solution for 2 hours. As depicted in Fig.18c, with the increase of exposure time of 5 hours in the solution, the pits were initiated randomly on the bent surface. It could be due to chromium-rich nitride precipitation (Fig.17) at the grain boundaries. The active galvanic sites for pit initiation are at the interface of the austenite matrix and Cr_2N precipitates. Further increased exposure time in the solution leads to the formation of more corrosion pits by anodic dissolution, as shown in Fig.18 (d-g). The SCC mechanism was initiated by the anodic dissolution between the anodic sites (chromium-depleted regions) and cathodic sites (austenite matrix), which are the source of the initiation of corrosion pits. Figure 19 shows the surface morphologies on the U bend specimen exposed for 150 hrs in 45% $MgCl_2$ solution and clearly shows evidence of localized intergranular attack at the pitting sites. The localized attack may lead to IGSCC failure due to the synergistic action of susceptible microstructure, tensile stress, and corrosive environment (Ref 58]. Kumar et al. (Ref 59] reported similar findings on the metals susceptible to SCC and highly influenced by their microstructural properties. When exposed to chloride ions, the HNASS material exhibits a self-protective behavior by creating a passive protective layer of chromium oxide. However, the protective film of the U-bend specimen may be ruptured by slip bands caused by the plastic deformation induced by constant strain (Ref 60, 61].

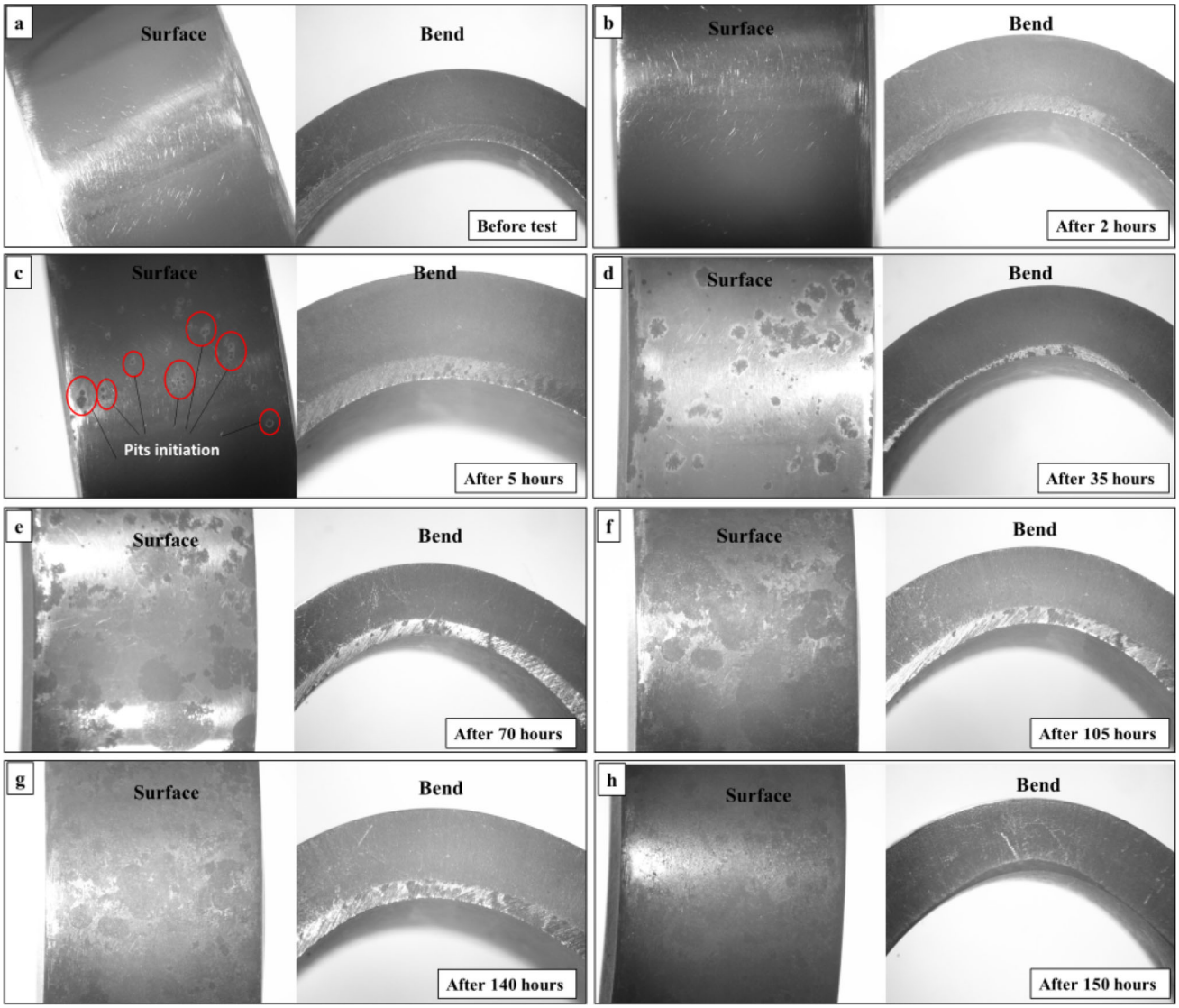

Fig. 18 Macroscopic observations at 10x on the U bend surface of HNASS aged at 750 °C for 1 hour exposed to a boiling 45% MgCl2 solution for 150 hours

From the present study, the corrosion behavior of the nickel and molybdenum-free high nitrogen austenitic stainless steel (HNASS) is affected by several factors, such as chemical composition, exposure to elevated temperature, duration of exposure time, susceptible microstructure, tensile stresses, and the corrosive environment. It was found that, the correlation is established between the microstructural morphology, % DOS, pitting, and SCC behavior of HNASS. The above phenomena is evident and expressed as follows: As the alloy is isothermal aged within the aging range resulted in various morphologies of (fine, discrete, and globular) Cr_2N precipitates along the grain boundaries at lower ageing temperature. Whereas the lamellar Cr_2N (false pearlite) formed within the grain interior at higher ageing temperature when exposed for a longer duration. The initiation of pitting corrosion is influenced by the presence of Cr_2N precipitates, which are mainly in the vicinity of grain boundaries. In the corrosive environment, as exposure time increases more corrosion pits are formed at the active sites due to galvanic interaction between Cr_2N precipitates and austenite matrix. These active sites are the primary source for anodic path dissolution for pitting corrosion and the possible SCC mechanism in HNASS.

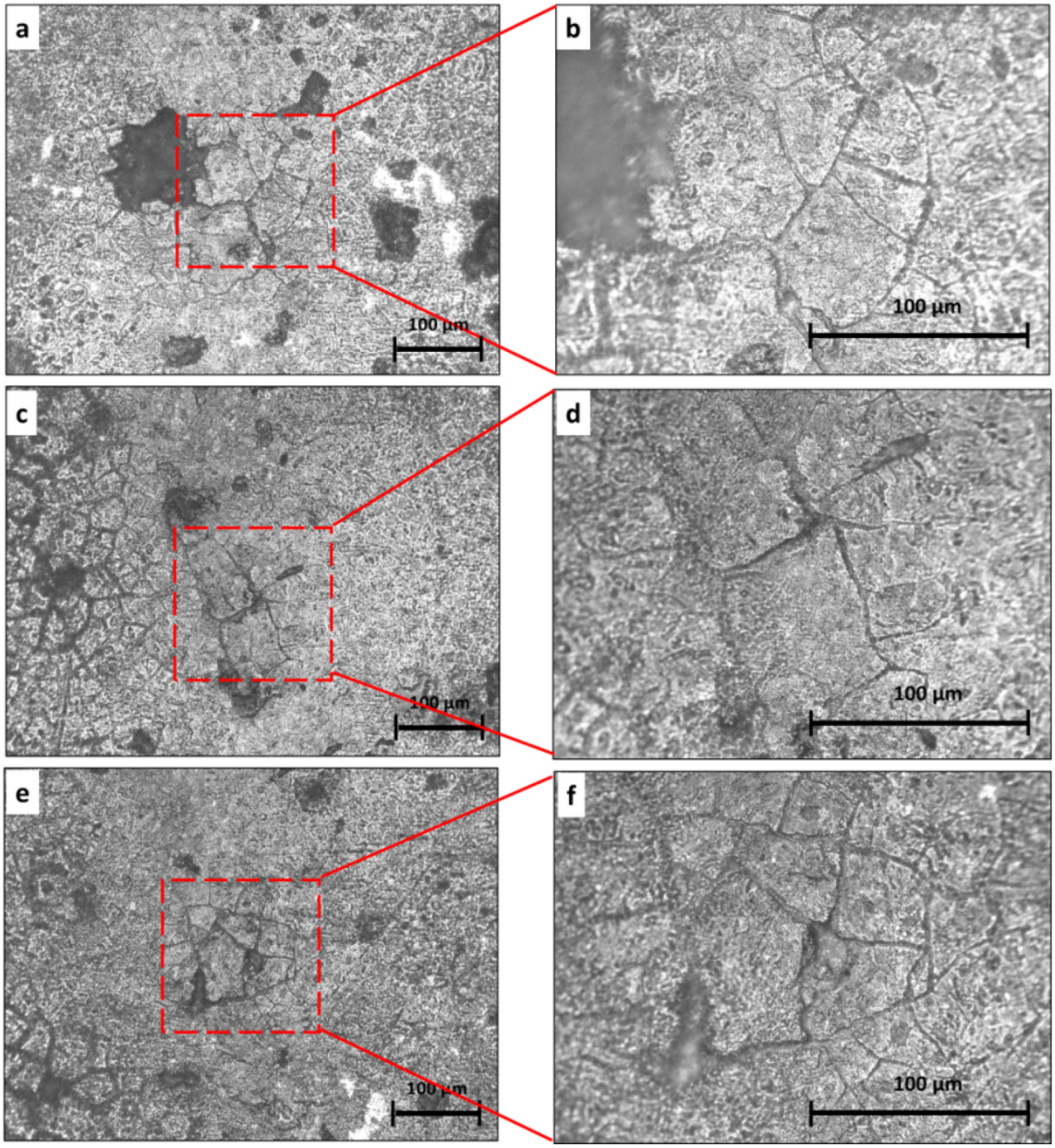

Fig. 19 Micrographs on the bent surface of HNASS aged at 750 °C for 1 hour exposed to a boiling 45% $MgCl_2$ solution for 150 hours

4. Conclusions

- The nickel and molybdenum-free high nitrogen austenitic stainless-steel (HNASS) microstructure in the solutionized condition is found to have an austenite matrix with annealed twins near the grain boundaries. Isothermal ageing at the sensitization110 range resulted in HNASS acting as a precipitate-sensitive material along with aging temperature and exposure duration.
- Fine, globular, and discrete Cr_2N precipitation is observed at grain boundaries when the alloy is treated at 550 °C for all exposure durations and 650 °C, 750 °C, and 850 °C for lower exposure duration. The lamellar Cr_2N pearlite-like microstructure was formed within the austenite grain when treated at 650 °C, 750 °C, and 850 °C after 360 min, 180 min, and 60 min, respectively.
- From the DL-EPR and PDP studies, higher % DOS (52.52%) and lower Epit (− 252.36 mV) at an isothermal temperature of 850 °C for 720 min exposure time are observed. However, the alloy exhibited lower % DOS (47.06% at 750 °C for 1440 min and 43.71% at 850 °C for 1440 min) and higher Epit (− 157.95 mV at 750 °C for 1440 min and − 153.191 mV at 850 °C for 1440 min) in DL-EPR and PDP studies due to the insufficient depletion of chromium (Cr) content caused by nitride precipitation at the exposure after 720 min at 750 °C, and 850 °C.
- The SCC behavior of HNASS was investigated in an aged condition at 750 °C for 1 hour and exposed to a boiling 45% $MgCl_2$ solution for 150 hours. During the test, no visible cracks were identified on the bent surface. The SCC mechanism was initiated by the anodic dissolution

between the anodic sites (chromium-depleted regions) and cathodic sites (austenite matrix), which are the source of the initiation of corrosion pits.
- The present study established that HNASS treated at isothermal ageing conditions are affected by various morphologies of Cr_2N precipitation formed at the grain boundaries and within the matrix and are correlated with the intergranular, pitting, and stress corrosion cracking behaviour.

Acknowledgments

The authors sincerely thank the Director of NIT Andhra Pradesh for providing funds under the Research Seed Grant (RSG) for this study. The authors thank Dr. G Madhusudhan Reddy, Former Director, DMRL, for his continuous support and encouragement in the work.

References

1. J.W. Simmons, D.G. Atteridge, and J.C. Rawers, Sensitization of High-Nitrogen Austenitic Stainless Steels by Dichromium Nitride Precipitation. United States. https://doi.org/10.5006/1.3294349 (1994)
2. M. Kikuchi and Y. Mishima, High nitrogen steels, in Proceedings of the Conference on High Nitrogen Steels (HNS '95), Kioto, Japan, (1996)
3. R. Mohammed, G.M. Reddy, and K.S. Rao, Effect of Filler Wire Composition on Microstructure and Pitting Corrosion of Nickel Free High Nitrogen Stainless-steel GTA Welds, *Trans. Indian Inst. Met.*, 2016, **69**(10), p 1919–1927.
4. T.B. Gibbons, Recent Advances in Steels for Coal Fired Power Plant: A Review, *Trans. Indian Inst. Met.*, 2013, **66**, p 631–640.
5. L. Huabing, J. Zhou-hua, Z. Zu-rui, C. Yang, and Y. Yan, Intergranular Corrosion Behavior of High-Nitrogen Austenitic Stainless-Steel, *International Journal of Minerals, Metallurgy and Materials*, 2009, **5**, p 654–660.
6. Y.S. Yoon, H.Y. Ha, T.H. Lee, and S. Kim, Effect of N and C on Stress Corrosion Cracking Susceptibility of Austenitic Fe18Cr10Mn-Based Stainless-Steels, *Corros. Sci.*, 2014, **80**, p 28–36.
7. R. Mohammed, G. Madhusudhan Reddy, and K. Srinivasa Rao, Welding of Nickel free High-Nitrogen Stainless-Steel: Microstructure and Mechanical Properties, *Def. Technol.*, 2017, **13**(2), p 59–71.
8. A. Di Schino and J.M. Kenny, Grain Refinement Strengthening of a Micro-Crystalline High-Nitrogen Austenitic Stainless-Steel, *Mater. Lett.*, 2003, **57**, p 1830–1834.
9. N. Nobuo, H. Naoki, T. Toshihiro, and T. Setsuo, Grain Refinement of Nickel-Free High-Nitrogen Austenitic Stainless-Steel by Reversion of Eutectoid Structure, *Scr. Mater.*, 2007, **57**, p 153–156.
10. S. Sheik, R. Mohammed, A. Tirumalla et al., Correlative Analysis of Morphology–Mechanical–Corrosion Behavior of Conventional Nickel-Based and Nitrogen-Alloyed Nickel-Free Austenitic Stainless-steels, *J. Mater. Eng. Perform.*, 2023, **32**, p 1196–1212.
11. F. Shi, X. Zhang, T. Li, X. Guan, X. Li, and C. Liu, Effects of Nitrogen Content and Strain Rate on the Tensile Behavior of High-Nitrogen and Nickel-Free Austenitic Stainless Steel, *Crystals*, 2023, **13**(1), p 129.
12. H. Hänninen, J. Romu, R. Ilola, J. Tervo, and A. Laitinen, Effects of Processing and Manufacturing of High-Nitrogen-Containing Stainless-Steels on their Mechanical, Corrosion and Wear Properties, *J. Mater. Process. Technol.*, 2001, **117**, p 424–430.
13. H. Baba, T. Kodama, and Y. Katada, Role of Nitrogen on the Corrosion Behavior of Austenitic Stainless-Steels, *Corros. Sci.*, 2002, **44**, p 2393–2407.
14. I. Olefjord and L. Wegrelius, The Influence of Nitrogen on the Passivation of Stainless-Steels, *Corros. Sci.*, 1996, **38**, p 1203–1220.
15. M.G. Pujar, U.K. Mudali, and S.S. Singh, Electrochemical Noise Studies of the Effect of Nitrogen on Pitting Corrosion Resistance of High-Nitrogen Austenitic Stainless-Steels, *Corros. Sci.*, 2011, **53**, p 4178–4186.
16. F. Gao, Y. Qiao, J. Chen et al., Effect of Nitrogen Content on Corrosion Behavior of High-Nitrogen Austenitic Stainless Steel, *NPJ Mater. Degrad.*, 2023, **7**, p 75.
17. S. Xu, F. Gao, J. Han, S. Xiong, X. Duan, F. Zha, B. Yu, L. Yang, Y. Qiao, Z. Zheng et al., Corrosion Behaviors of Fe-22Cr-16Mn-0.55N High-Nitrogen Austenitic Stainless Steel in 3.5% NaCl Solution, *Coatings*, 2022, **12**, p 1769.
18. M. Metikos-Hukovi, C.R. Babic, Z. Grubac, Z. Petrovic, and N. Lajci, High Corrosion Resistance of Austenitic Stainless-Steel Alloyed with Nitrogen in an Acid Solution, *Corros. Sci*, 2011, **53**, p 2176–2183.
19. T. Anita, S. Vani, R.P. George, and J. Philip, Effect of Nitrogen on the Intergranular Stress Corrosion Cracking Resistance of 316LN Stainless Steel, *Corrosion.*, 2020, **76**, p 693.
20. S. Kolli, V. Javaheri, J. Kömi, and D. Porter, On the Role of Grain Size and Carbon Content on the Sensitization and Desensitization Behavior of 301 Austenitic Stainless Steel, *Metals*, 2019, **9**, p 1193.
21. S. Rahimi, and T.J. Marrow, A New Method for Predicting Susceptibility of Austenitic Stainless Steels to Intergranular Stress Corrosion Cracking, *Mater. Des.*, 2020, **187**, p 108368.
22. S. Kolli et al., The Importance of Steel Chemistry and Thermal History on the Sensitization Behavior in Austenitic Stainless Steels: Experimental and Modeling Assessment, *Mater. Today Commun.*, 2020, **24**, p 101088.
23. H. Li, Z. Jiang, H. Feng, Q. Ma, and D. Zhan, Aging Precipitation Behavior of 18Cr-16Mn-2Mo-llN High Nitrogen Austenitic Stainless-steel and Its Influences on Mechanical Properties, *J. Iron. Steel. Inst.*, 2012, **19**(8), p 43–51.
24. B. Kartik, R. Veerababu, M. Sundararaman, and D.V.V. Satyanarayana, Effect of High Temperature Aging on Microstructure and Mechanical properties of a Nickel-free High Nitrogen Austenitic Stainless-steel, *Mater. Sci. Eng. A*, 2015, **642**, p 288–296.
25. T.-H. Lee, C.-S. Oh, C.G. Lee, S.-J. Kim, and S. Takaki, Precipitation of r-Phase in High-Nitrogen Austenitic 18Cr–18Mn–2Mo–0.9 N Stainless-Steel During Isothermal Aging, *Scr. Mater.*, 2004, **50**, p 1325–1328.
26. W. Xinqiang, F. Yao, J. Huang, E. Han, W. Ke, K. Yang, and Z. Jiang, Investigation on Pitting Corrosion of Nickel-Free and Manganese Alloyed High-Nitrogen Stainless-Steels, *J. Mater. Eng. Perform.*, 2009, **18**, p 287–298.
27. P. Rosemann, C. Müller, and T. Halle, Sensitization Behaviour of the Nitrogen Alloyed Austenitic Stainless Steel X8CrMnMoN18-19-2, in IOP Conference Series: Materials Science and Engineering. Vol. 882. No. 1. IOP Publishing, (2020)
28. K.K. Krishna, J. Anburaj, R. Dhanasekar et al., Kinetics of Cr_2N Precipitation and Its Effect on Pitting Corrosion of Nickel-Free High-Nitrogen Austenitic Stainless-Steel, *J. Mater. Eng. Perform.*, 2020, **29**, p 6044–6052.
29. F. Shi, Y. Qi, and C. Liu, Effects of Mo on the Precipitation Behaviors in High-Nitrogen Austenitic Stainless-Steels, *J. Mater. Sci. Technol.*, 2011, **27**(12), p 1125–1130.
30. Y. Qiao, X. Wang, L. Yang, X. Wang, J. Chen, Z. Wang, H. Zhou, J. Zou, and F. Wang, Effect of Aging Treatment on Microstructure and Corrosion Behavior of a Fe-18Cr-15Mn-0.66N Stainless-Steel, *J. Mater. Sci. Technol.*, 2022, **107**, p 197–206.
31. H. Li, Z. Jiang, H. Feng, Q. Ma, and D. Zhan, Aging Precipitation Behavior of 18Cr-16Mn-2Mo-1.1N High Nitrogen Austenitic Stainless-steel and Its Influences on Mechanical Properties, *J. Iron Steel Res. Int.*, 2012, **19**(8), p 43–51.
32. L. Hu, H. Peng, I. Baker, L. Li, W. Zhang, and T. Ngai, Characterization of High-Strength High-Nitrogen Austenitic Stainless-Steel Synthesized from Nitrided Powders by Spark Plasma Sintering, *Mater. Charact.*, 2019, **152**, p 76–84.
33. H. Li, Z. Jiang, Z. Zhang, Y. Cao, and Y. Yang, Intergranular Corrosion Behavior of High Nitrogen Austenitic Stainless Steel, *Int. J. Miner. Metall. Mater.*, 2009, **16**, p 654–660.
34. T.H. Lee, S.J. Kim, and Y.C. Jung, Crystallographic Details of Precipitates in Fe-22Cr-21Ni-6Mo-(N) Superaustenitic Stainless-Steels Aged at 900 °C, *Metall. Mater. Trans. A*, 2000, **31**, p 1713–1723.
35. N. Kauss, A. Heyn, O. Michael, M. Schymura, and P. Rosemann, Application Limits and Sensitisation Behaviour of the Manganese- and Nitrogen-Alloyed Austenitic Stainless Steel P2000 (X13CrMnMoN18-14-3), *Mater. Corros.*, 2021, **72**, p 1656–1667.

36. A. Devasenapathi and M. Asawa, Effect of High Mn on SCC Behaviour of an Austenitic Stainless Steel in 42% Boiling $MgCl_2$ Solution, *J. Mater. Sci. Lett.*, 1997, **16**, p 1363–1365.
37. A. Osama and R. Nishimura, On the SCC Behaviour of Austenitic Stainless Steels in Boiling Saturated Magnesium Chloride Solution, *Corros. Control Serv. Soc.*, 2007, **1**, p 257–266.
38. M. Raffi, K. Srinivasa Rao, and G. Madhusudhan Reddy, Effect of Microstructure on Stress Corrosion Cracking Behaviour of High Nitrogen Stainless Steel Gas Tungsten Arc Welds, in IOP Conference Series: Materials Science and Engineering. Vol. 330. No. 1. IOP Publishing (2018)
39. Y. Young-Sub et al., Comparative Study of Stress Corrosion Cracking Susceptibility of Fe18Cr10Mn-and Fe18Cr10Mn1Ni-Based High Nitrogen Stainless Steels, *Corros. Sci.*, 2014, **88**, p 337–348.
40. Q. Yanxin et al., Effect of Aging Treatment on Microstructure and Corrosion Behavior of a Fe-18Cr-15Mn-0.66 N Stainless-Steel, *J. Mater. Sci. Technol.*, 2022, **107**, p 197–206.
41. H. Ha and H. Kwon, Effects of Cr_2N on the Pitting Corrosion of High Nitrogen Stainless-Steels, *Electrochim. Acta*, 2007, **52**(5), p 2175–2180.
42. J. Wu, Y. Qiao, Y. Chen et al., Correlation between Corrosion Films and Corrosion-Related Defects Formed on 316 Stainless-steel at High Temperatures in Pressurized Water, *J. Mater. Eng. Perform.*, 2021, **30**, p 3577–3585.
43. ASTM International, Technical Standard ASTM G108-15, ASTM International, West Conshohocken, PA 2015
44. N. Parvathavarthini and U.K. Mudali, Electrochemical Techniques for Estimating the Degree of Sensitization in Austenitic Stainless steels, *Corros. Rev.*, 2014, **32**, p 5–6. https://doi.org/10.1515/corrrev-2014-0029
45. ASTM G36-94. Standard practice for evaluating stress-corrosion-cracking resistance of metals and alloys in a boiling magnesium chloride solution. West Conshohocken, PA: ASTM International; 2018. 2018 www.astm.org
46. ASTM G30-97. Standard practice for making and using U-bend stress-corrosion test samples. West Conshohocken, PA: ASTM International; 1997. Available from: www.astm.org
47. R. Mohammed, M.G. Reddy, and K.R. Srinivasa, Microstructure and Pitting Corrosion of Shielded Metal Arc Welded High Nitrogen Stainless-Steel, *Def. Technol.*, 2015, **11**(3), p 237–243.
48. N. Parvathavarthini and R.K. Dayal, Influence of Chemical Composition, Prior Deformation and Prolonged Thermal Aging on the Aging Characteristics of Austenitic Stainless-Steels, *J. Nucl. Phys. Mater. Sci. Radiat. Appl.*, 2002, **305**, p 209–219.
49. Z.X. Zhang, Y.P. Liang, H.P. Qu, J.Z. Xiang, Z.X. Zhang, Y.P. Liang, H.P. Qu, and J.Z. Xiang, Research on Microstructure and Properties of Cr-Mn-N Austenitic Stainless-Steel for Non-magnetic Drilling Collar Application, *Hot Work. Technol.*, 2013, **18**(42), p 147–152.
50. M. Sun, Y. Yang, M. Luo, L. Jiang, Y. Jiang, and J. Li, Investigation of Susceptibility to Intergranular Corrosion of Tin-Added Austenitic Stainless-Steel, *Acta Metall. Sin-Engl*, 2015, **28**, p 1183–1189.
51. T. Sourmail, C.H. Too, and H.K.D.H. Bhadeshia, Sensitisation and Evolution of Chromium-Depleted Zones in Fe-Cr-Ni-C SYSTEMS, *ISIJ Int.*, 2003, **43**, p 1814–1820.
52. W. Zhou, W. Ma, Y. Li, and Y. Sun, Effect of Sensitizing Treatment on the Microstructure and Susceptibility to Intergranular Corrosion of High-Nitrogen Austenitic Stainless-steel, *Metall. Microstruct. Anal.*, 2021, **10**(1), p 25–35.
53. P. Chung and S. Szklarska-Smialowska, The Effect of Heat Treatment on the Degree of sensitization of Type 304 Stainless-steel, *Corrosion*, 1981, **37**(1), p 39–50.
54. P.O. Atanda, A. Fatudimu, and O. Oluwole. Sensitisation study of normalized 316L stainless-steel. (2010)
55. S. Kolli, T. Ohligschläger, J. Kömi, and D. Porter, Aging and Self-healing in Austenitic Stainless-Steel: Quantitative Prediction Considering Carbide Nucleation and Growth, *ISIJ Int.*, 2019, **5**, p 86.
56. P.K. Gajjar, B.C. Khatri, A.M. Siddhpura et al., Aging and Deaging (Healing) in Austenitic Stainless-steel: A Critical Review, *Trans. Indian Inst. Met.*, 2022, **75**, p 1411–1427.
57. S.M. Bruemmer, L.A. Chariot and B.W. Arey, Aging Development in Austenitic Stainless-steel: Correlation between STEM-EDS and EPR Measurements, *Corrosion*, 1988, **44**(6), p 328–333.
58. K.R. Trethewey, Some Observations on the Current Status in the Understanding of Stress-Corrosion Cracking of Stainless-Steels, *Mater. Des.*, 2008, **29**(2), p 501–507.
59. S.R. Kumar, K. Gudimetla, P. Venkatachalam et al., Stress Corrosion Cracking of Al7075 Alloy Processed by Equal Channel Angular Pressing, *Int. J. Eng. Sci. Technol.*, 2010, **2**, p 53–61.
60. R.H. Jones, *Stress Corrosion Cracking*, ASM International, Ohio, 1992
61. V.S. Raja and T. Shoji, *Stress Corrosion Cracking Theory and Practice*, Woodhead Publishing Limited, Cambridge, 2011